

AD/A-006 236

SOLID ROCKET MOTOR INSPECTION BY  
ACOUSTICAL HOLOGRAPHY TECHNIQUES

Dale Collins

Holosonics, Incorporated

Prepared for:

Air Force Rocket Propulsion Laboratory

January 1975

DISTRIBUTED BY:

**NTIS**

National Technical Information Service  
U. S. DEPARTMENT OF COMMERCE

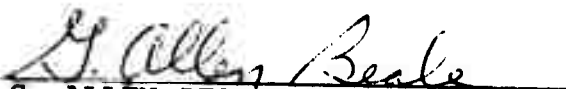
## NOTICES

When U.S. Government drawings, specifications, or other data are used for any purpose other than a definitely related government procurement operation, the Government thereby incurs no responsibility nor any obligation whatsoever, and the fact that the Government may have formulated, furnished, or in any way supplied the said drawings, specifications or other data, is not to be regarded by implication or otherwise, or in any manner licensing the holder or any other person or corporation, or conveying any rights or permission to manufacture, use, or sell any potential invention that may in any way be related thereto.

## FOREWORD


This report was submitted by Holosonics, Inc., 2950 George Washington Way, Richland, Washington 99352, under Contract No. FO4611-74-C-0019, Job Order No. 197000BE with the Air Force Rocket Propulsion Laboratory, Edwards, CA 93523.

This report has been reviewed by the Information Office/DOZ and is releasable to the National Technical Information Service (NTIS). At NTIS it will be available to the general public, including foreign nations.

  
G. ALLEN BEALE, GS-13  
Project Engineer

FOR THE COMMANDER

  
P. J. DAILY, Colonel, USAF  
Chief, Technology Division

  
WILLIAM D. SIURU, MAJOR USAF  
Chief, Supporting Technology  
Branch

A

**UNCLASSIFIED**

SECURITY CLASSIFICATION OF THIS PAGE (When Data Entered)

REPORT DOCUMENTATION PAGE		READ INSTRUCTIONS BEFORE COMPLETING FORM
1. REPORT NUMBER AFRPL TR-74-83	2. GOVT ACCESSION NO.	3. RECIPIENT'S CATALOG NUMBER
4. TITLE (and Subtitle) Solid Rocket Motor Inspection by Acoustical Holography Techniques		5. TYPE OF REPORT & PERIOD COVERED Final Report
		6. PERFORMING ORG. REPORT NUMBER
7. AUTHOR(s) Dr. Dale Collins		8. CONTRACT OR GRANT NUMBER(s) F04611-74-C-0019
9. PERFORMING ORGANIZATION NAME AND ADDRESS Holosonics, Inc. 2950 George Washington Way Richland WA 99352		10. PROGRAM ELEMENT, PROJECT, TASK AREA & WORK UNIT NUMBERS
11. CONTROLLING OFFICE NAME AND ADDRESS Air Force Rocket Propulsion Laboratory Director of Science and Technology Air Force Systems Command Edwards AFB CA 93523		12. REPORT DATE January 1975
14. MONITORING AGENCY NAME & ADDRESS (if different from Controlling Office)		13. NUMBER OF PAGES 58
		15. SECURITY CLASS. (of this report) Unclassified
		15a. DECLASSIFICATION/DOWNGRADING SCHEDULE N/A
16. DISTRIBUTION STATEMENT (of this Report) Approved for public release; distribution unlimited		
17. DISTRIBUTION STATEMENT (of the abstract entered in Block 20, if different from Report)		
18. SUPPLEMENTARY NOTES		
19. KEY WORDS (Continue on reverse side if necessary and identify by block number) Nondestructive Testing                      Solid Rocket Motors Ultrasonics                                      Solid Propellant Acoustical Holography Holography Service Life		
20. ABSTRACT (Continue on reverse side if necessary and identify by block number) The feasibility of using acoustical holography as a nondestructive technique for determining small innerbore cracks and debonds in larger solid rocket motors was demonstrated. Cracks as small as one inch long, one-half inch deep, and less than 0.002" thick located on the innerbore of a simulated Minuteman third stage motor (18" web-thickness) were readily identified. Unbonds of one square inch area between the case and propellant were imaged.		

DD FORM 1 JAN 73 1473 ED

Reproduced by  
NATIONAL TECHNICAL  
INFORMATION SERVICE  
US Department of Commerce  
Springfield, VA. 22151

**UNCLASSIFIED PRICES SUBJECT TO CHANGE**  
SECURITY CLASSIFICATION OF THIS PAGE (When Data Entered)

## CONTENTS

Section 1	INTRODUCTION AND SUMMARY
	1.1 Objectives
	1.2 Background
	1.3 Test Samples
	1.4 Summary
Section 2	THEORY AND DESIGN OF THE DEBOND DETECTION AND IMAGING SYSTEM
	2.1 General Theory
	2.2 Resonance Frequency Selection Principles
	2.3 Simplified Wave Form Analysis of the Resonance Section
Section 3	EXPERIMENTAL RESULTS OF DEBOND IMAGING IN SOLID PROPELLANT MOTOR SECTIONS
	3.1 Titanium Case Debond Imaging Results
Section 4	BASIC DESIGN CRITERIA FOR IMAGING RADIAL CRACKS IN SOLID PROPELLANT
Section 5	HOLOGRAPHIC IMAGING SYSTEM
	5.1 General Description
	5.2 Operation
	5.3 Radial Crack Imaging Resolution and Geometry
	5.4 Effective Innerbore Scanning Aperture
	5.5 Image Resolution
	5.6 Rayleigh Resolution
	5.7 Resolution - (Experimental Results)
	5.8 Radial Crack Focused Holography Resolution Imaging
	5.9 Resolution Simulation Geometry for the Fiber Glass Case Sample
	5.10 Simulated Radial Crack Imaging
	5.11 Radial Crack Imaging on Rocket Motor Sections
	5.12 Radial Crack Imaging Sensitivity
	5.13 Simplified Radial Crack Image Analysis
Section 6	CONCLUSIONS
	REFERENCES

## SECTION 1

### INTRODUCTION AND SUMMARY

#### 1.1 *Objectives*

The objectives of this program were to determine the feasibility of using acoustical holography techniques to 1) detect and image radial cracks located on the innerbore of a large solid rocket motor and, 2) to detect and image case/liner/ propellant debonds in solid rocket motors.

#### 1.2 *Background*

There are no current methods of inspecting large solid rocket motors in confined spaces such as a Minuteman Missile stored in a silo. Techniques are available to X-ray and bore scope inspect motors, however, this requires a time consuming and costly removal and dismantling of the missile at the silo site and transporting the motor to a central location for inspection. Several recent studies in the evaluation of nondestructive inspection techniques have indicated that acoustical (or ultrasonic) methods would provide a means of surveying the rocket motor internally for cracks and debonds. Acoustical holography techniques have been used successfully in the past to provide high resolution images of defects in various materials. Prior to this effort no attempt had been made to image through 18 inches of solid rocket propellant.

#### 1.3 *Test Samples*

Three test specimens were provided by the Air Force for the feasibility study using the acoustical holography method. The specimens were representative of the three motor stages of the Minuteman Missile (MM).

The first sample had a fiber glass case 0.28 inches thick bonded to an 18 inch ANB 3066 (Carboxyterminated Poly-butadiene/Ammonium Perchlorate/Aluminum) solid propellant. This segment was actually cut from a MM motor and was 52 inches in diameter and 36 inches high. The innerbore was scraped to a smooth cylindrical surface in order to enhance the feasibility study by removing one of the variables, a rough surface.

The second sample also was cut from an actual MM motor and consisted of a titanium case 0.12 inches thick with 18 inches of ANB 3066 propellant. The sample was 52 inches in diameter and 36 inches high. The bore was scraped to a smooth cylindrical surface.

The third sample was specially prepared to simulate a first stage MM motor. It consisted of a steel case 0.08 inches thick bonded to a 14 inch ANB 3066 propellant web. The sample was 45 inches in diameter and 36 inches high. The bore was cast to a smooth cylindrical form.

#### 1.4 *Summary*

The theoretical and experimental results of this program are:

1.4.1 The ability to detect and image small radial flaws or cracks emanating from the innerbore of a solid rocket motor section. The detection and holographic imaging is accomplished from the external fiber glass surface of the rocket motor.

1.4.2 The ability to penetrate and image through 18 inches of rocket propellant at 160KHz employing send-receive techniques from the external surface.

1.4.3 Flaw or crack detect resolution (send-receive operation) is 0.5 inches at the innerbore. (i.e., at 18 inches depth)

1.4.4 Flaw or crack imaging resolution is approximately 1.8 inches at the innerbore.

1.4.5 The ability to detect and image case/liner/propellant debonds in the titanium Minuteman rocket motor sections.

1.4.6 Debond (cross-sectional area) detectable resolution is approximately  $0.14\text{in}^2$  to  $0.16\text{in}^2$ .

## SECTION 2

### THEORY AND DESIGN OF THE DEBOND DETECTION AND IMAGING SYSTEM

#### 2.1 General Theory

The acoustical method employed to detect and image case/liner/propellant debonds is the resonance technique. This technique utilizes the acoustic compressional waves transmitted into the rocket motor's external surface from a single source-receiver transducer. The frequency is either pre-selected by calculating the fundamental resonance of the external motor case material or varied manually or electronically until the resonance occurs. Standing waves will now occur within the metal or titanium case, causing it to resonate or vibrate at a larger amplitude. Figure 1 shows the simplified transducer/case geometry for the resonance technique.

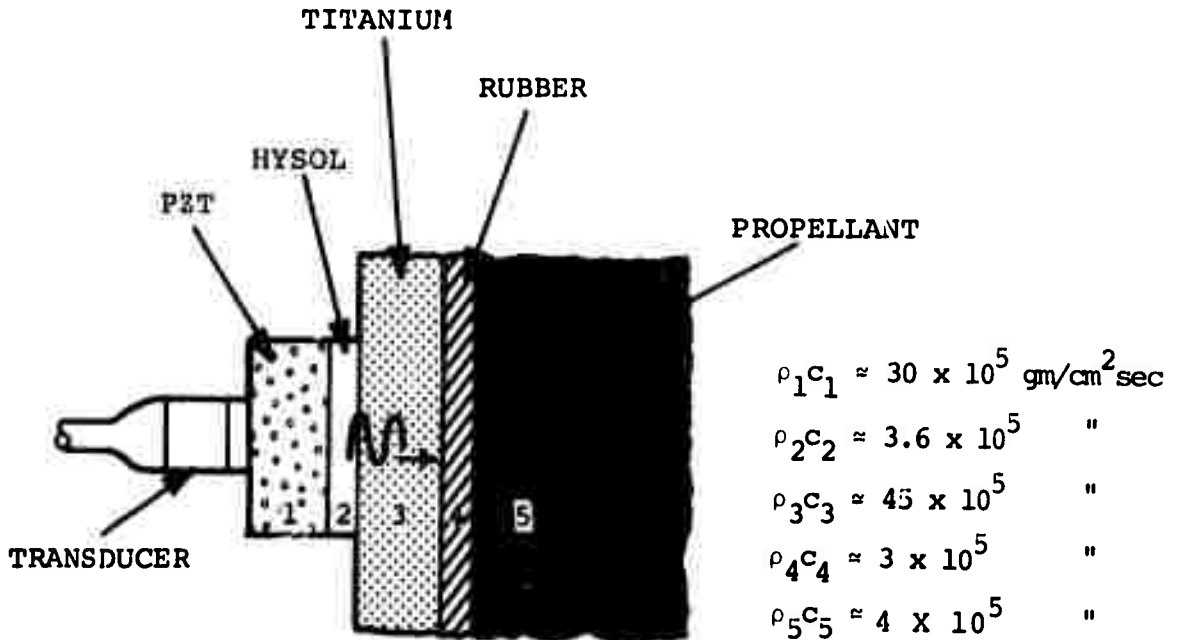


FIGURE 1. TRANSDUCER/CASE GEOMETRY



If a debond occurs between the steel or titanium and rubber interface, the transducer will excite the composite section and set up standing waves in the medium. Equation 1 represents two plane waves traveling to the right and left with pressure amplitudes  $P_1$  and  $P_2$ . These two pressure amplitudes are usually not equal and may be complex quantities

$$p = P_1 e^{j(\omega t - \beta x)} + P_2 e^{j(\omega t + \beta x)} \quad (1)$$

where  $\omega$  = radian frequency

and  $\beta$  = wave number.

The particle velocity is easily obtained from Equation 1 and using the following relationship between particle displacement and pressure gradient.

$$U_x = \frac{1}{\rho_0 c} \left\{ P_1 e^{j(\omega t - \beta x)} - P_2 e^{j(\omega t + \beta x)} \right\} \quad (2)$$

where  $-\frac{\partial p}{\partial x} = \rho_0 \frac{\partial^2 \xi}{\partial t^2} = j\omega \rho_0 U_x$ .

The specific acoustic impedance is defined as the complex ratio of the sound pressure to the particle velocity, at a given point, in the wave field.

$$Z_{sp} = \frac{p}{u} = \rho_0 c \left( \frac{P_1 e^{-j\beta x} + P_2 e^{j\beta x}}{P_1 e^{-j\beta x} - P_2 e^{j\beta x}} \right) = \rho_0 c \gamma. \quad (3)$$

Now let us consider plane waves in an ideal rigid section of the motor case with uniform cross-sectional dimensions, small compared with the wavelength. The section is also assumed to be rigidly terminated at the boundary, thus forcing the particle velocity ( $U_x$ ) to be zero at  $x = a$ .

$$\gamma = \frac{e^{j\beta(a-x)} + e^{-j\beta(a-x)}}{e^{j\beta(a-x)} - e^{-j\beta(a-x)}} = -j \frac{\cos \beta(a-x)}{\sin \beta(a-x)} \quad (4)$$

The impedance assumes all values from  $-j\infty$  to  $+j\infty$  each time the distance is increased by a half wavelength (i.e.,  $a-x = \lambda/2, 2\lambda/2, 3\lambda/2, \dots$ ). The sound wave sees an infinite impedance or stiffness at the titanium/air interface (i.e.,  $a-x = 0$ ). The air gap represents a debond between the titanium/rubber interface. The impedance decreases to zero as  $a-x$  approaches  $\lambda/4$ . The fundamental resonance thickness is  $\lambda/2$  for the various composite rocket motor cases (steel, titanium, etc.).

The impedance at  $\lambda/2$  is infinite and can be considered either infinite mass or an infinite stiffness. The sequence is repeated every subsequent half wavelength. Theoretically, the energy should remain in this section forever, but in reality there is always resistance in the system. The "Q" of the system is by definition:

$$Q = 2\pi \frac{\text{energy stored in L}}{\text{energy dissipated per cycle in R}} \quad (5)$$

and converting to the equivalent mechanical circuit elements:

$$Q = \frac{\omega_0 \text{Mass}}{\text{Damping}} \quad (6)$$

The "Q" of the system approaches infinity every half wavelength (i.e.,  $M \rightarrow \infty$ ). The wave train at resonance will be essentially undamped with the titanium or steel/air debonds.

## 2.2 Resonance Frequency Selection Principles

The fundamental resonance frequency ( $f_0$ ) in the thickness direction of the case section is given by the following equation:

$$f_0 = \frac{c}{2t} \quad (7)$$

where  $t$  is the thickness of the section, and  $c$  the acoustic velocity. Fundamental resonance occurs where the case thickness equals  $\lambda/2$ . The higher harmonics are easily calculated for subsequent half wavelengths in the section.

$$f_n = \frac{nc}{2t} \quad (8)$$

where  $(n = 1, 2, \dots)$ .

Figure 2 illustrates the conditions for resonance.

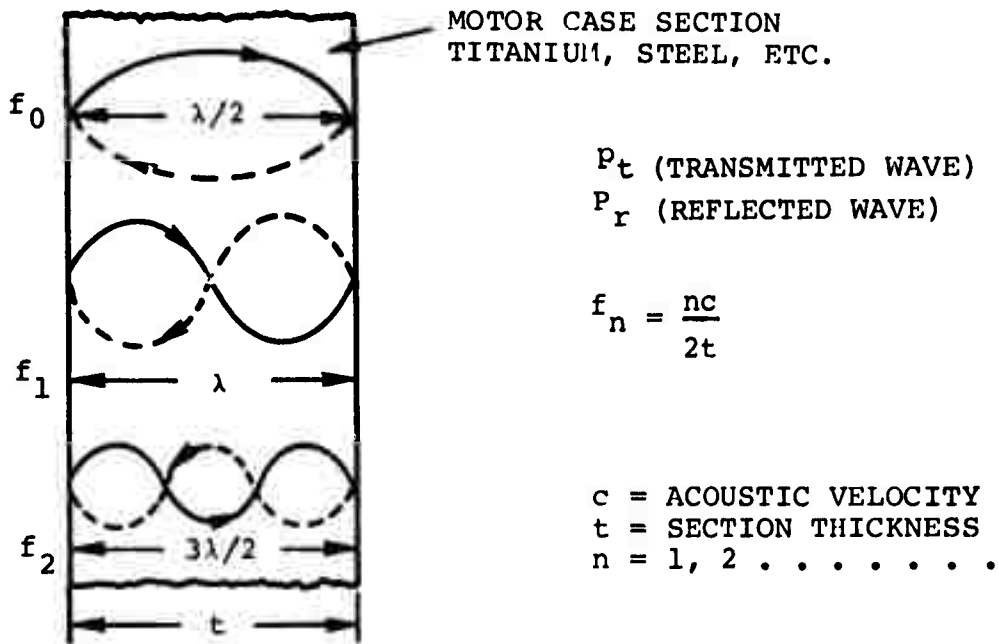


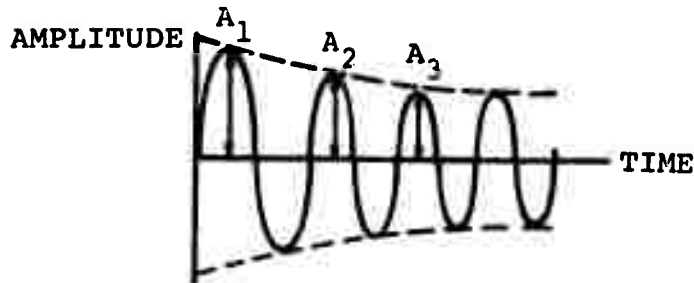
FIGURE 2. CONDITION FOR RESONANCE IN THE ROCKET MOTOR

### 2.3 Simplified Wave Form Analysis of the Resonance Section

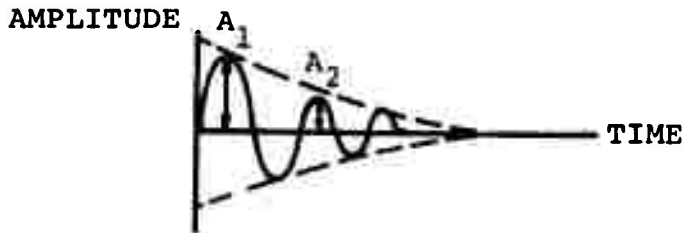
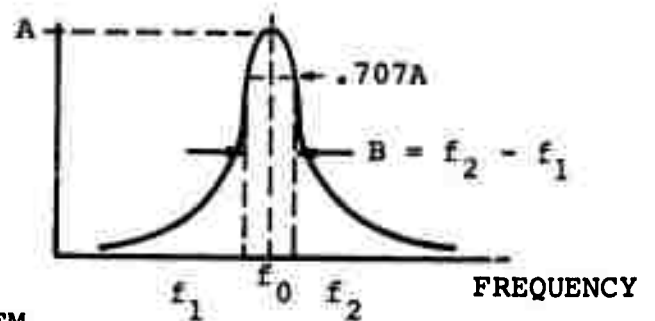
The resultant shape of the damped or undamped sinusoid is used to evaluate the "Q" of the system and hence the debond detection sensitivity. Figure 3 shows an example of two different wave forms with their resultant "Q"s and frequency band widths.

$$\xi = \frac{A_1}{A_2} = \frac{A_2}{A_3} = \frac{A_n}{A_{n+1}}$$

$$Q = \frac{f_0}{f_2 - f_1} \cong \frac{\pi}{\ln \xi}$$



(a) HIGH "Q" SYSTEM



(b) LOW "Q" SYSTEM

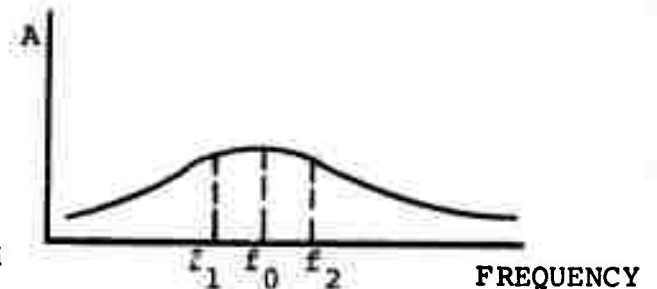


FIGURE 3. ACOUSTIC WAVE FORMS WITH RESPECT TO THE "Q" OF THEIR SYSTEMS (a) high "Q" system and (b) low "Q" system

The titanium or steel/air debond will exhibit a high "Q" as shown in Figure 3a. The value of  $\xi$  the damping factor can be defined in terms of the plane wave acoustic impedances of the coupling materials if we accept a simple analysis.

Figure 4' shows the simplified geometry of three materials with two interfaces.

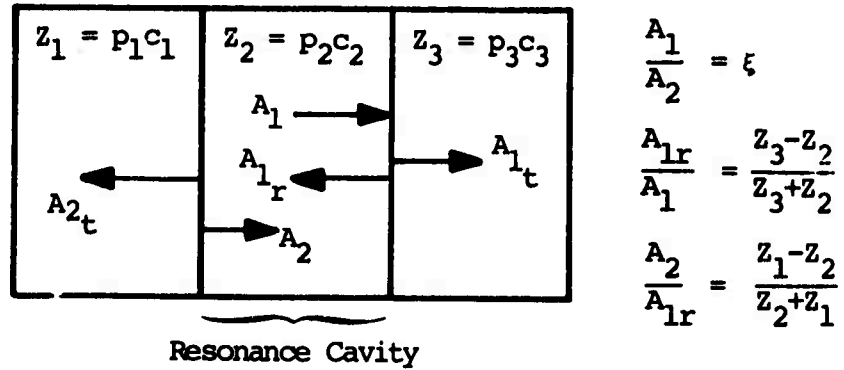


FIGURE 4. SIMPLE GEOMETRY FOR DERIVING THE DAMPING FACTOR  $\xi$

The damping factor is defined as the ratio of the internal pressure wave amplitude ( $A_1$ ), to the second wave twice reflected, as shown in Figure 4.

The damping factor or coefficient can then be expressed mathematically by the following equation:

$$\xi = \frac{A_1}{A_2} = \frac{A_2}{A_3} = \frac{A_n}{A_{n+1}} \approx \left( \frac{Z_3 + Z_2}{Z_3 - Z_2} \right) \left( \frac{Z_2 + Z_1}{Z_1 - Z_2} \right) \quad (9)$$

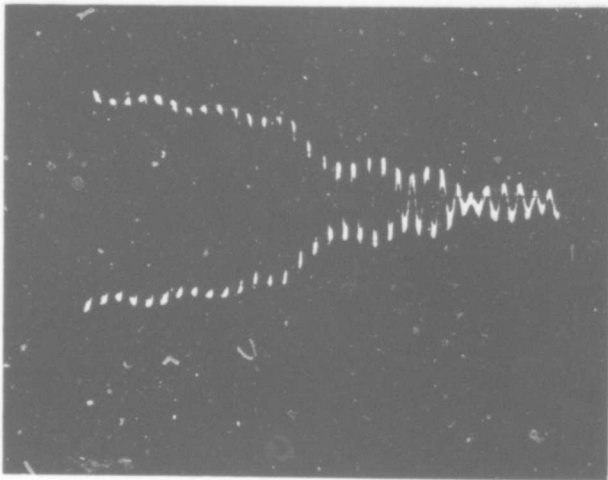


FIGURE 5a. TRANSDUCER OVER FLAW FREE AREA ON THE MOTOR SECTION

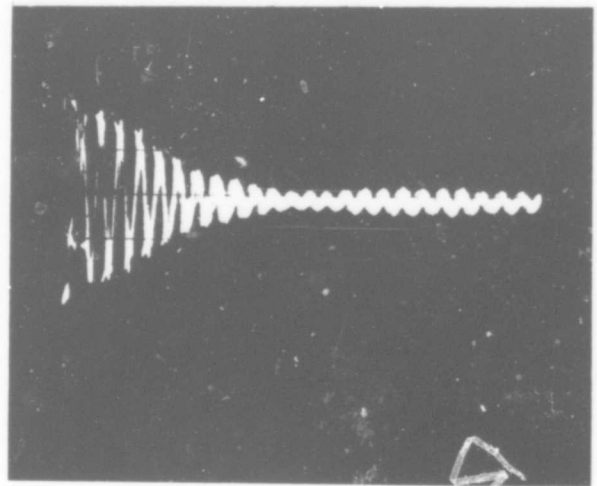


FIGURE 5b. TRANSDUCER NOT IN CONTACT WITH MOTOR SECTION (LEAD META-NIOBATE)

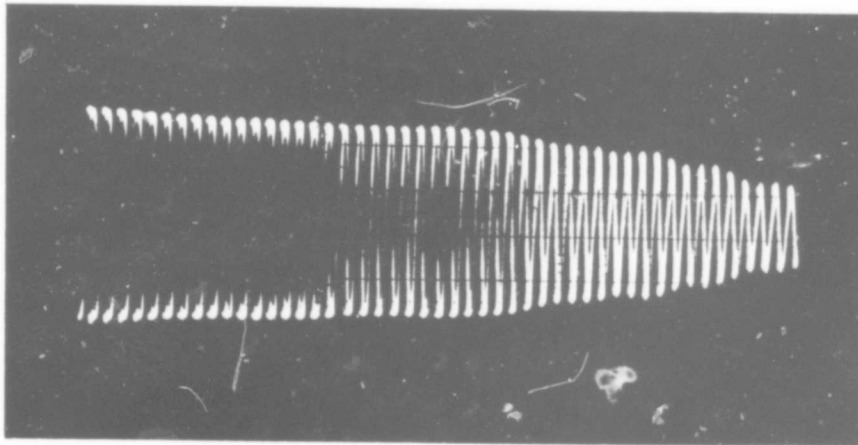


FIGURE 5c. TRANSDUCER OVER FLAW AREA ON MOTOR SECTION

The quality factor or "Q" is defined by the following expression<sup>(1)</sup>:

$$Q \approx \frac{\pi}{\ln \xi} \quad (10)$$

It can also be defined in terms of the resonance curve as shown in Figure 3a (i.e.,  $Q = f_0/B$ ).

Figures 5 a,b, & c illustrate the various wave forms obtained in one of debond resonance tests. The external skin or metal thickness is 0.08 inches with 0.4 inches thickness of rubber bonded to the internal surface. The geometry is shown in Figure 6.

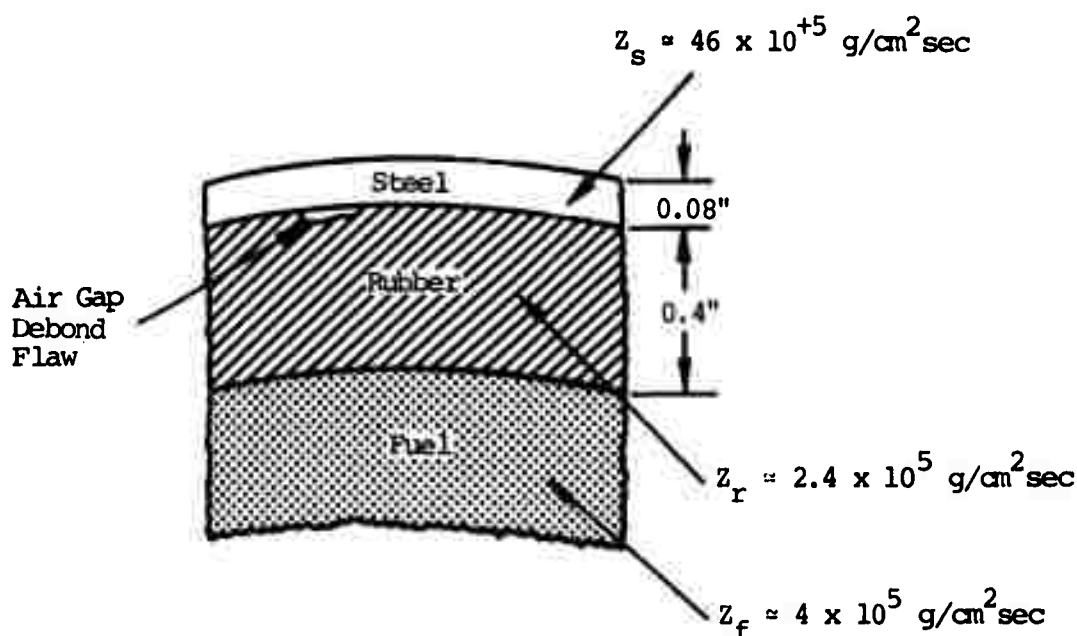


FIGURE 6. SOLID ROCKET MOTOR SAMPLE CROSS-SECTIONAL GEOMETRY

The fundamental resonance was calculated using Equation 7 and verified experimentally to be 1.44MHz. The variation in the "Q" or quality factor was calculated using the experimental data. The "Q" of the debond-free section was ap-

proximately 12 and with the debond section 76. The "Q" varied by a factor of six between the two areas.

Figure 5b is the wave form of the lead meta-niobate transducer in air. The internal damping factor ( $\xi$ ) for lead meta-niobate is 1.3 and the experimental value from the wave form analysis was approximately 1.4 indicating excellent correlation. Figure 5a shows the effect of coupling the transducer to the motor surface showing the increase in the apparent "Q" (i.e., a decrease in  $\xi$ ). The resonance test provides excellent detection of debonds at the case/rubber and rubber/fuel interfaces by exhibiting large variations in the quality factor of the motor section.



### SECTION 3

#### EXPERIMENTAL RESULTS OF DEBOND IMAGING IN SOLID PROPELLANT MOTOR SECTIONS

The preliminary experimental results were obtained on simulated inert rocket motor sections. The interface debonds (case/rubber, rubber/fuel) were imaged with excellent quality on the inert samples. All of the images were constructed using the manual scanner in conjunction with the HolScan Signal Processor. Figure 7 shows a simplified diagram and picture of the experimental apparatus used in constructing the debond images. The images were obtained by delaying the gate many cycles beyond the transmit pulse and detecting only the excessive ringing signal of the high "Q" debond area, as shown in Figures 5a and 5c. The signal amplitude in the gate over the debond-free area is extremely small and insufficient to trigger the detector. The detected debond signal is then amplified and drives the "Z" axis of the Tektronix 603 display scope. The image after signal processing appears on the tube face.

Three simulated debonds were constructed using the inert sample shown in Figure 8. The picture shows the bottom layer of inert propellant with three 0.75 inch holes. Two of the holes were drilled to simulate case/rubber debonds and the other to simulate a rubber/fuel debond. The holes were then plugged with RTV to prevent water leakage into the air gaps. Figure 9 shows the cross-sectional geometry of the three debonds. The debond images are shown in Figure 10. The lateral image magnification is 0.46 and the resolution approximately 0.75 inch. The images of the case/rubber debonds (a,c) and the rubber/fuel debond (b) are of excellent quality considering the area detection technique.

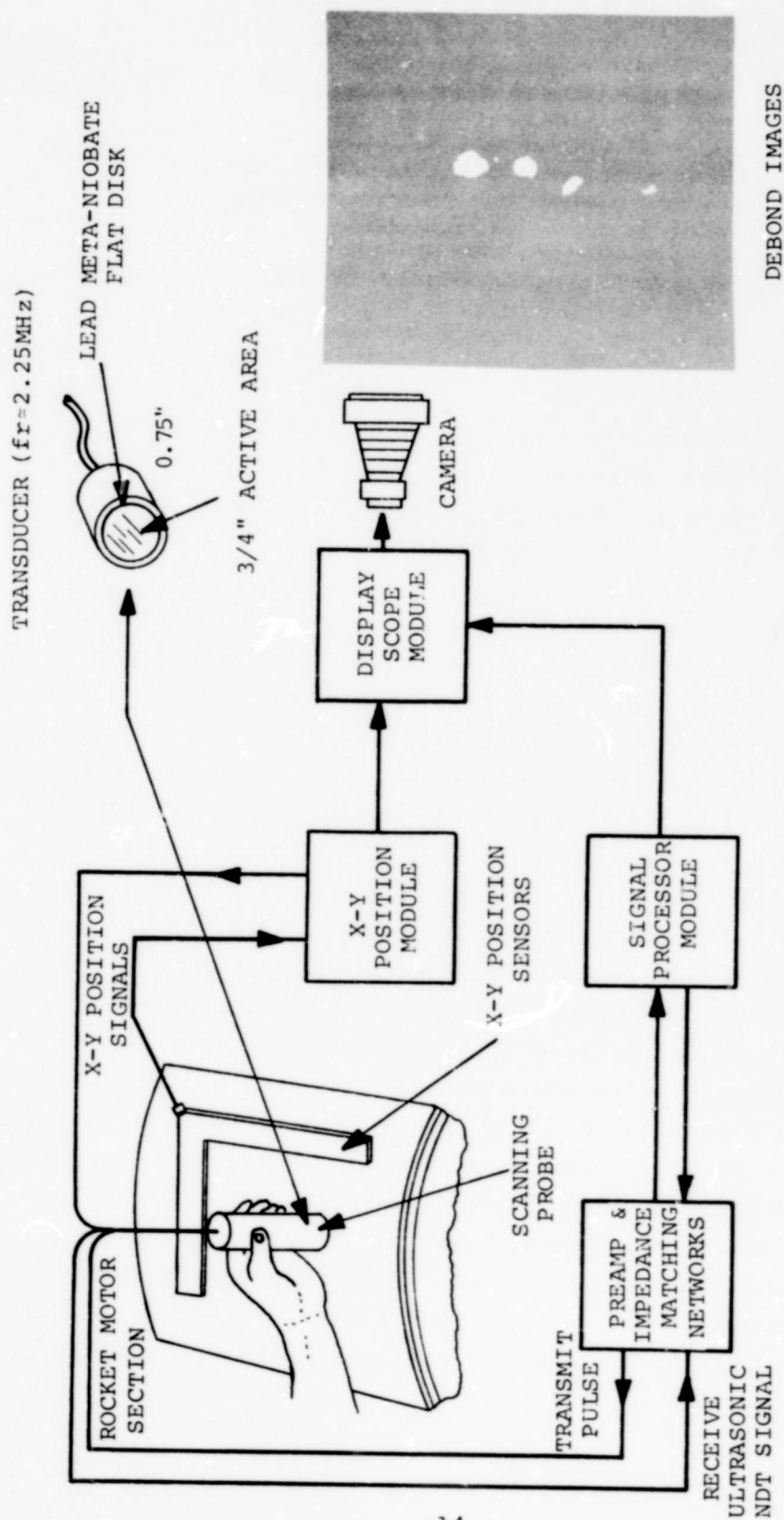


FIGURE 7. DEBOND MANUAL IMAGING SYSTEM

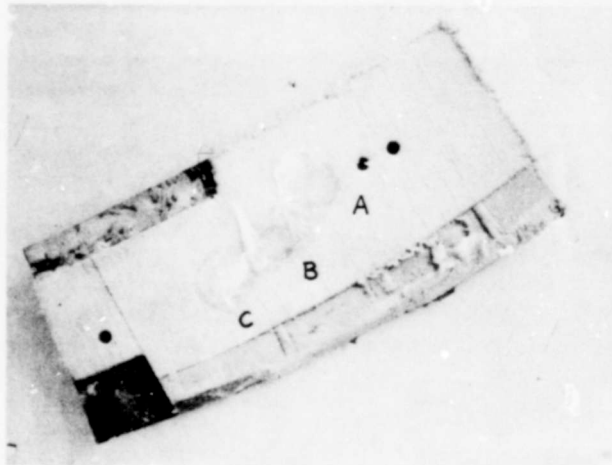


FIGURE 8. SIMULATED DEBONDS IN A SOLID ROCKET MOTOR SECTION (INERT)

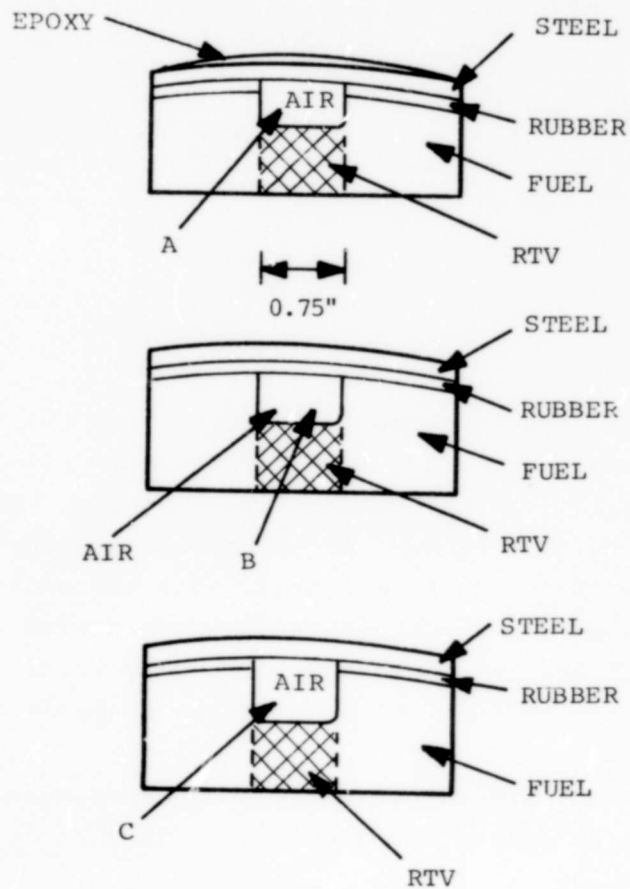
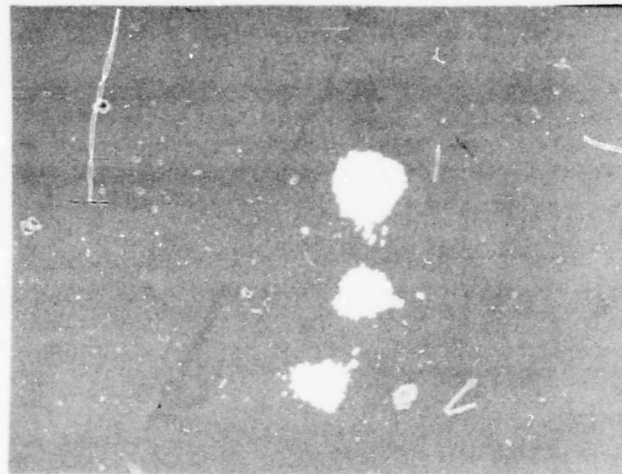


FIGURE 9. CROSS-SECTIONAL DEBOND GEOMETRY:  
(A,C) case/rubber debonds and  
(B) rubber/fuel debond



Flaw "A"

Flaw "B"

Flaw "C"

FIGURE 10. IMAGES OF DEBONDS IN SIMULATED  
INERT MOTOR SECTION: (A & C)  
case/rubber debonds and (B)  
rubber fuel debond  
Magnification: 0.46

### 3.1 *Titanium Case Debond Imaging Results*

The resonance technique was implemented into the HolScan Digital Mechanical Scanner System for the in situ tests on active propellant at the Yakima Firing Center. The manual scanner was omitted because of the inherent danger of the active spark (X-Y) position signal. The new units have deleted this active spark generation method with a ceramic (PZT) cylindrical transducer option. This eliminates the possible danger of ignition with active propellant.

The Digital Mechanical Scanner is shown in Figure 11 mounted on the titanium case motor section.

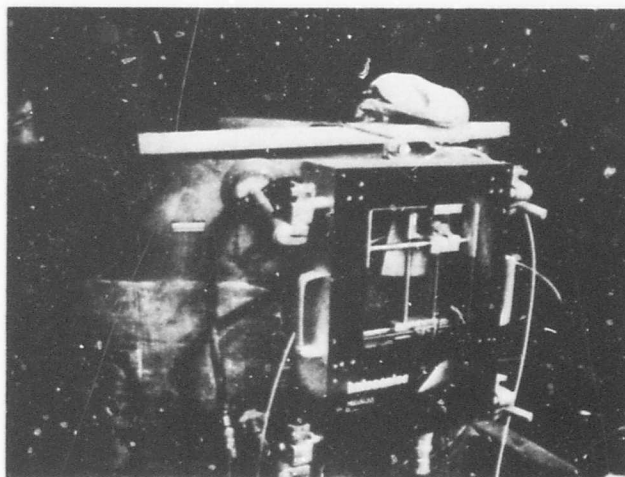


FIGURE 11. DEBOND DETECTION AND IMAGING  
SYSTEM ON THE TITANIUM CASE  
MOTOR SECTION

The attachment of the scanner to the motor case is through four vacuum feet which are connected by hoses to a vacuum pump. A special transducer coupler was designed to provide optimum coupling to the cylindrical surface for the resonance debond test. Figure 12 shows a diagram of the transducer coupler. The stainless steel bellows provides the flexible coupling between the rectilinear scanner and cylindrical surface. The acoustic coupling is obtained by pumping water or any compatible liquid into the transducer coupler. Figure 13 shows the titanium case motor section with the case/rubber interface debond geometry. The debond area was approximately  $1.9 \text{ in}^2$ .

The thickness of the titanium case was 0.12 inch resulting in a resonance frequency of 1.05MHz. The cork was omitted from the debond imaging, as it had been removed previously before shipment to Yakima. The signal processing was identical to the previous inert tests, except the Digital Mechanical Scanner was substituted for the manual scanner. Figure 14 shows the typical wave forms generated over the

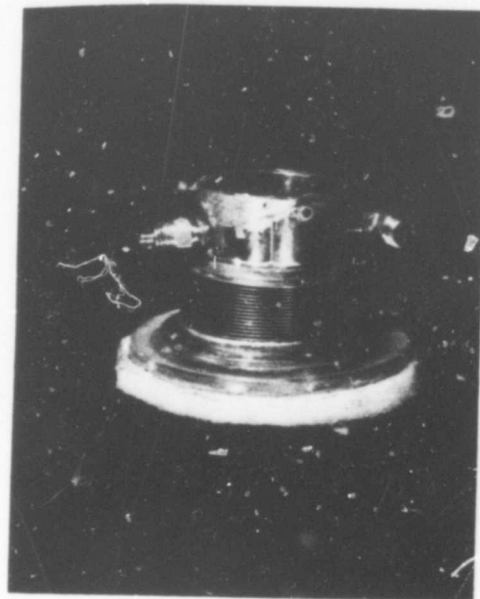
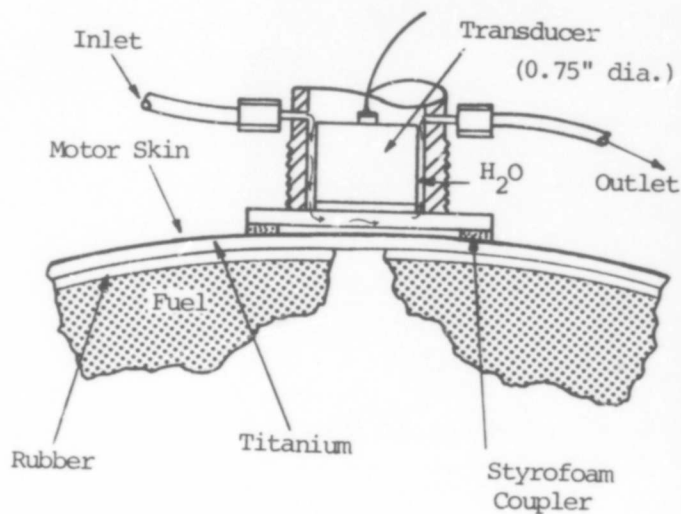


FIGURE 12. SIMPLIFIED DIAGRAM OF THE TRANSDUCER HOUSING FOR DEBOND IMAGING

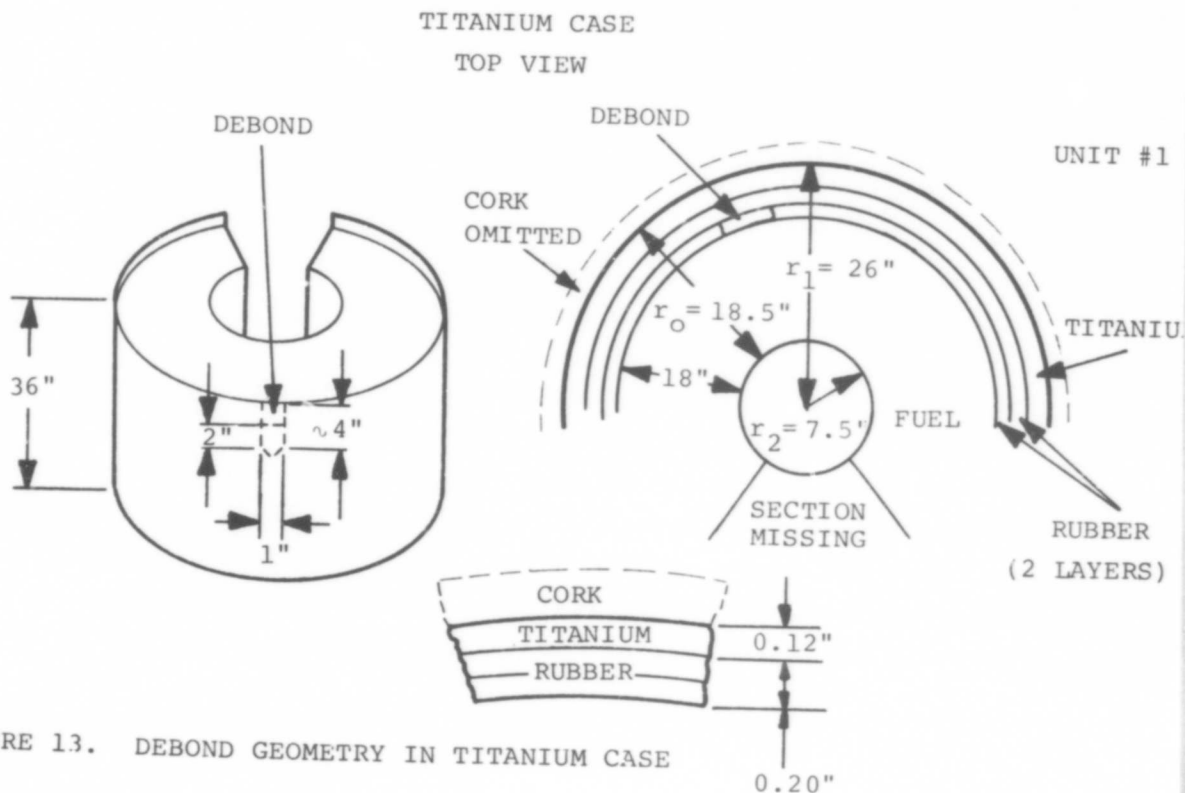
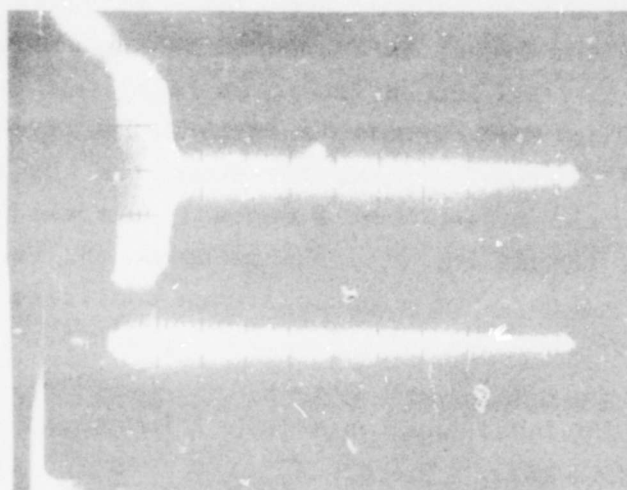


FIGURE 13. DEBOND GEOMETRY IN TITANIUM CASE

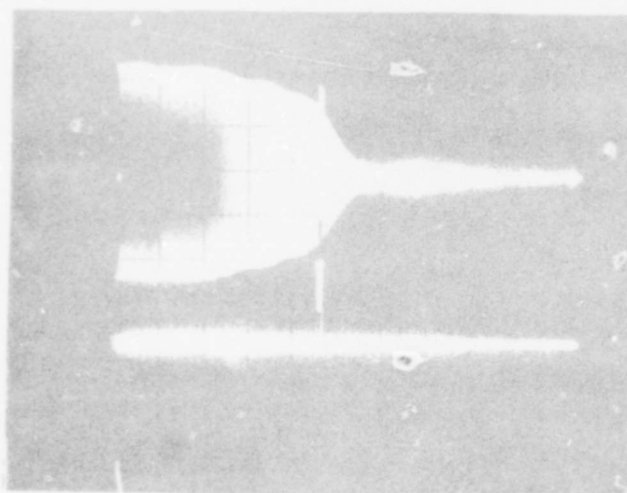
debond free area (a) and the debond area (b). The small pedestal represents the signal gate imposed on the acoustic signal (upper trace). The debond free area signal (a) is excessively damped (low "Q" circuit) and the signal gate is delayed beyond this ringing. Figure 14b shows the signal ringing, indicating the presence of a debond. The signal now extends in time beyond the gate and is detected, as shown in the lower trace. The signal is then amplified and conditioned to drive the Z axis of the display scope. Figure 15 shows the image of the titanium case debond. The actual size of the debond is approximately 2 inches in length and 1 inch in width. The debond size measured from the image (0.46 magnification) is 2.16 inches by 1.4 inches.



DEBOND FREE AREA  
WAVE FORM

DETECTED SIGNAL

(a)



DEBOND AREA WAVE  
FORM

DETECTED SIGNAL

(b)

FIGURE 14. TYPICAL DEBOND SIGNAL WAVE FORMS: (a) Debond free area wave forms (low Q) and (b) Debond area wave forms (high Q)





FIGURE 15. IMAGE OF DEBOND (CASE/RUBBER  
INTERFACE) IN TITANIUM CASE  
ROCKET MOTOR

Magnification: 0.46

## SECTION 4

### BASIC DESIGN CRITERIA FOR IMAGING RADIAL CRACKS IN SOLID PROPELLANT

Imaging small radial cracks emanating from the innerbore through approximately 18 inches of propellant presents stringent requirements on the acoustic imaging system. The crack's extremely small acoustic cross-section, when viewed directly above it, prevents any possibility of detection with the available operating frequencies. The major problem to circumvent is the extremely high attenuation exhibited by the solid rocket propellant. Typical values are shown in Figure 16 and range from 2db/in. to 10db/in. at 100KHz and 500KHz respectively. At 500KHz the signal would be attenuated by three million over the 36 inch propellant path. This physical characteristic of the propellant dictates the use of lower frequencies and higher powers. Naturally, lower frequencies imply longer wavelengths and decreasing resolution.

The optimum imaging system should operate at the highest possible frequency and maximum signal-to-noise ratio in conjunction with the signal power density. The above criteria impose one major physical limitation - namely possible cavitation in the transducer couplant. To avoid cavitation requires large area transducers resulting in low power densities in the couplant. If we employ large area plane wave transducers, the imaging system suffers dramatically in resolution, power density, and angular object illumination. One possible solution to the dilemma is the use of large area (low f number) focused transducers with their focal points at or near the inner motor bore. The large area reduces the possibility of couplant cavitation and the focal point at the innerbore surface provides the dramatic increase in object power density.

### Attenuation of the C-4 Propellant

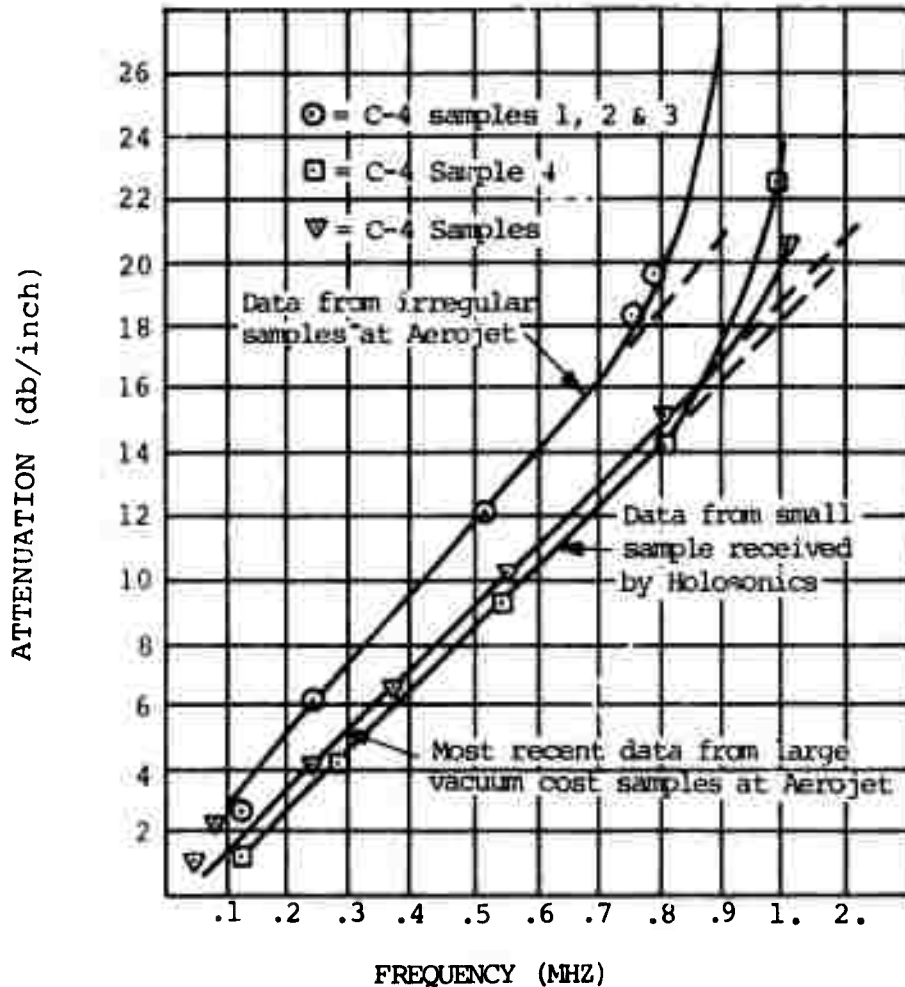


FIGURE 16. ATTENUATION CURVES FOR SOLID ROCKET PROPELLANT

The one remaining criterion - namely maximum signal-to-noise ratio associated with innerbore radial cracks - requires off-axis illumination. The choice was to employ two identical transducers viewing the crack at approximately 21 degrees (central angle) from the vertical on each side. This provided the imaging system with an effective 42 degree angular view of the crack. The acoustic cross-section of the crack's side view is orders of magnitude above the top

view, thus providing a sufficiently detectable reflected signal for the system. The use of two transducers also avoids the usual signal interference in the pulse-echo mode from excessive ringing of the transmitter under high power excitation. The transmitter could be heavily damped to reduce the ringing, but not without the associated loss of sensitivity!

The imaging system was designed using the above criteria with one major additional factor to further improve the signal-to-noise ratio (i.e., focused holography). The low frequency PZT-4 transducers (thickness expanders) have a tendency to generate low frequency radial modes which interfere or mix with the higher frequency flaw signals. The multiple frequency noise is easily eliminated using focused holography (i.e., coherent detection). In the in situ tests at Yakima, coherent detection proved convincingly that low frequency noise would have voided the imaging without this technique.

In the above discussion, the description of the focused transducers was omitted. The ideal optimum configuration would provide an infinite depth of focus without resolution degradation. This essentially says the flaw could vary in depth and always be in focus without loss of resolution. The above statement simply describes a focusing device analogous to the optical axicon<sup>2</sup>. Acoustical axicons for medical applications (higher frequency) have been constructed and tested with excellent results<sup>3,4</sup>.

Acoustical axicons were designed at the lower frequencies for this project. Penn Engineering of Florida attempted to construct two prototypes, but failed because of thermal peripheral cracking. The effort was discontinued and large area lens transducers were substituted in the system. Future research should consider this type of focusing device for propellant imaging systems.

## SECTION 5

### HOLOGRAPHIC IMAGING SYSTEM

#### 5.1 *General Description*

The imaging system used in the construction of longitudinal focused holograms for the inspection of radial cracks in the motor segments is shown in Figure 17. Figure 17a shows the cylindrical scanner with the two transducers mounted against the exterior surface of the motor. The transducers have plastic shoes that provide acoustic coupling between the transducer and the case. A variable speed pump supplies the coupling liquid into each shoe. A pair of return lines prevents air entrapment in the liquid. The shoes have individual sealant gaskets that prevent loss of couplant.

The scanning head configuration (Figure 17b) shows the two transducers spring loaded against the case surface. The upper and lower rails provide the circular scanning track around the motor periphery. A d.c. motor (variable speed) drives the scanning head along the track providing the aperture width (i.e., x dimension). A digital stepping motor is used to increment the scanning head in either the y direction. The scanner controls enable the operator to program preselected apertures over the motor surface.

#### 5.2 *Operation*

Figure 18 is a simplified diagram of the focused holographic imaging system. The operation is similar to the HolScan NDT System used at higher frequencies. The various holographic imaging techniques with this system are discussed in depth in the following reference.<sup>(5)</sup> A brief description of the salient features of the rocket motor radial crack imaging system will be discussed.

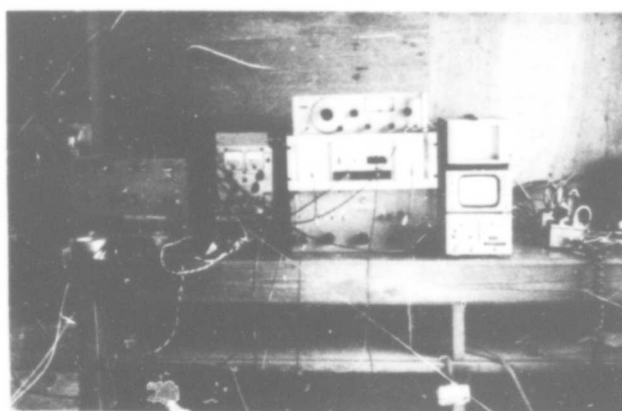
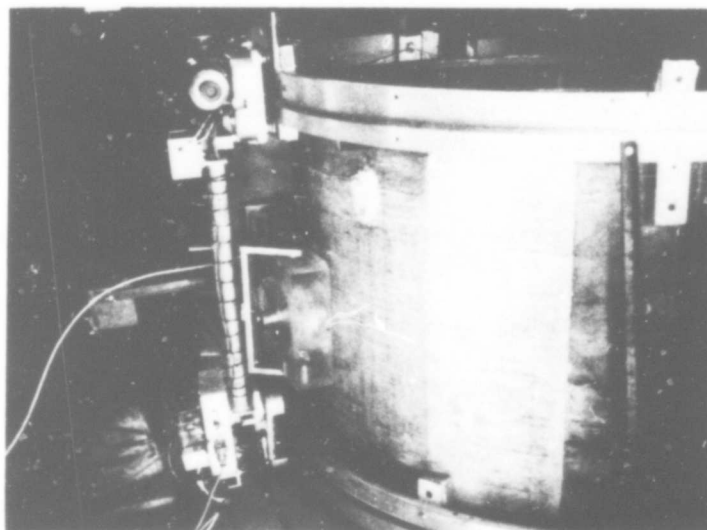
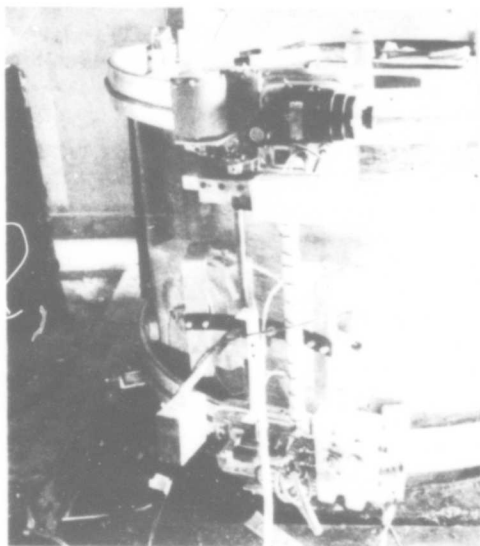


FIGURE 17. HOLOGRAPHIC IMAGING SYSTEM ON MINUTEMAN ROCKET  
MOTOR SECTION: (a) front view of cylindrical  
scanner with transducers, (b) side view of  
scanner and (c) signal processor with associated  
electronics

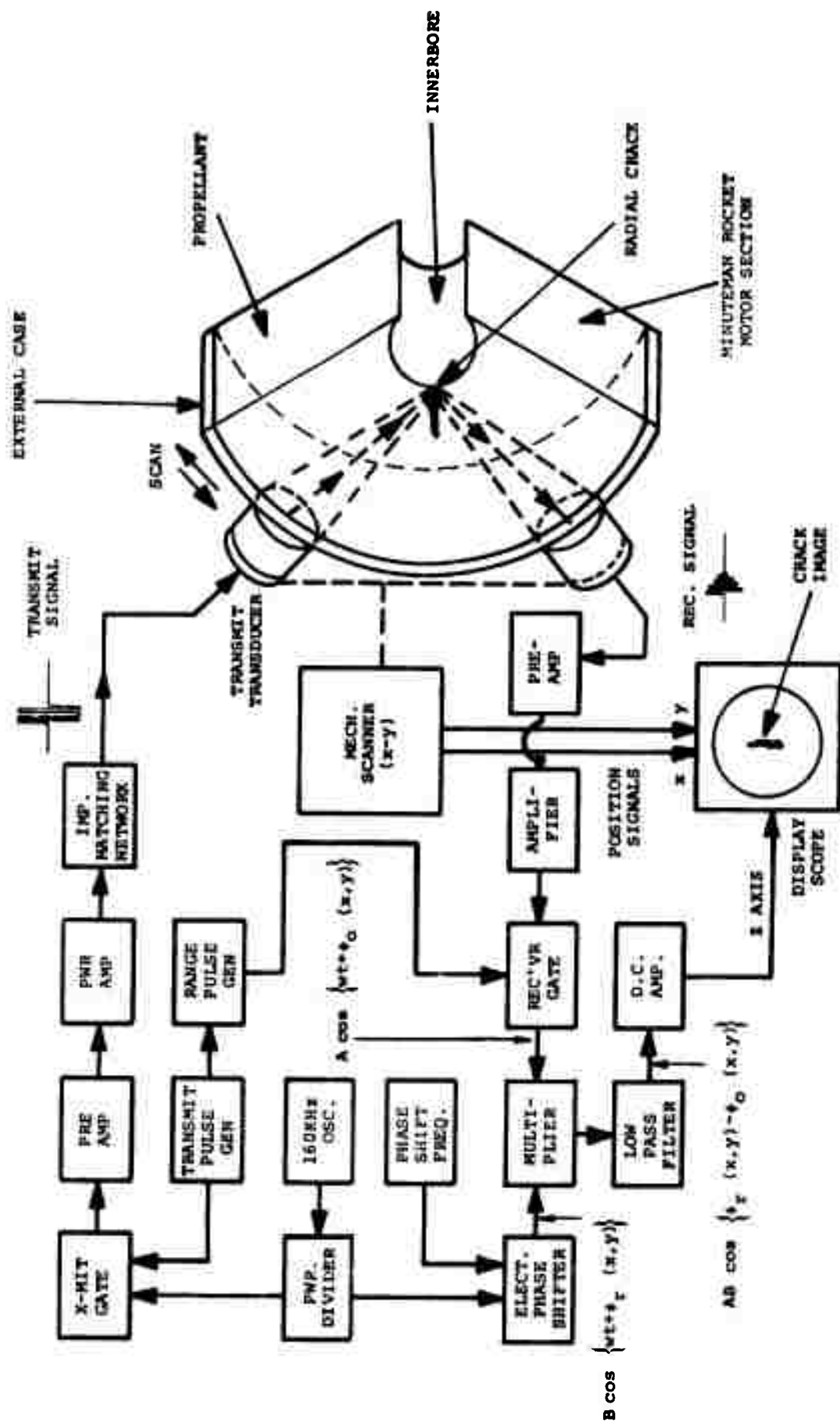


FIGURE 18. SIMPLIFIED BLOCK DIAGRAM OF THE HOLOGRAPHIC SYSTEM FOR IMAGING RADIAL CRACKS IN MINUTEMAN ROCKET MOTORS

The most expedient method of describing the system is to follow the signal from the start (i.e., oscillator) to the final image display. Figure 18 shows the 160KHz oscillator which represents the coherent source being divided or split into two signals, the object and reference, which parallels optical holography. The object signal is gated to produce short pulses which are then amplified and drive the source transducer after the impedance matching networks. The quasi-coherent electrical signal is converted into an acoustic pulse which insonifies the crack at the innerbore. The acoustic energy is focused at the innerbore increasing the power density by a factor of 15. The power density at the innerbore is approximately  $13 \text{ watts/in}^2$  (assuming 50% transducer efficiency). If plane wave transducers were employed to generate the equivalent power density, the required source power would have increased from 50 watts to 750 watts. This would generate power densities in the couplant very close to the cavitation limit for continuous excitation.

The innerbore crack interferes with the transmission of acoustic energy to the receive transducer. The image of the crack is obtained by scanning a sufficient innerbore aperture. The received acoustic signals are converted into electrical signals and then amplified. The signals are gated, multiplied with the reference phase shifted signal at the multiplier or balanced mixer and time averaged (see Figure 18). The electronic reference simulates an off-axis acoustic reference signal and imposes a modulation on the object crack signal. The resultant signal, after coherent detection, is amplified and conditioned to control the intensity of the display oscilloscope. The image is constructed on the display scope in conjunction with the x-y receiver position signals. The aspect ratio of the oscilloscope is adjusted to compensate for image distortion, as a result of the cylindrical surface.



### 5.3 Radial Crack Imaging Resolution and Geometry

Figure 19 is the geometry of the two imaging transducers located on the external rocket motor surface. The central ray of each focused transducer views the radial crack at 21 degrees. The two beams overlap at the innerbore surface providing insonification of the defect. The overlap of the two focused beams forms an elliptical area which is scanned over the innerbore surface to produce the resultant defect image.

The incident angle of each transducer was inclined approximately five degrees from the vertical and the refracted ray six degrees. The ray convergent at the focal point diverge rapidly as the inclination angle increases. The motor's external cylindrical surface also distorts the ray convergence and decreases the system's resolution. These two factors were omitted in the resolution analysis.

### 5.4 Effective Innerbore Scanning Aperture

Figure 20 shows the relationship between the external and inner scanned apertures. The length of the aperture in the "y" direction is identical for both apertures, but varies as the ratio of the respective radii in the "X" direction.

$$S_{2x} = \left( \frac{r_2}{r_1} \right) S_{1x} \quad (1)$$

where  $S_{1x}$  = external aperture length in the "X" direction

$S_{2x}$  = innerbore aperture length in the "X" direction

$r_1$  = missile outer radius

$r_2$  = innerbore radius.

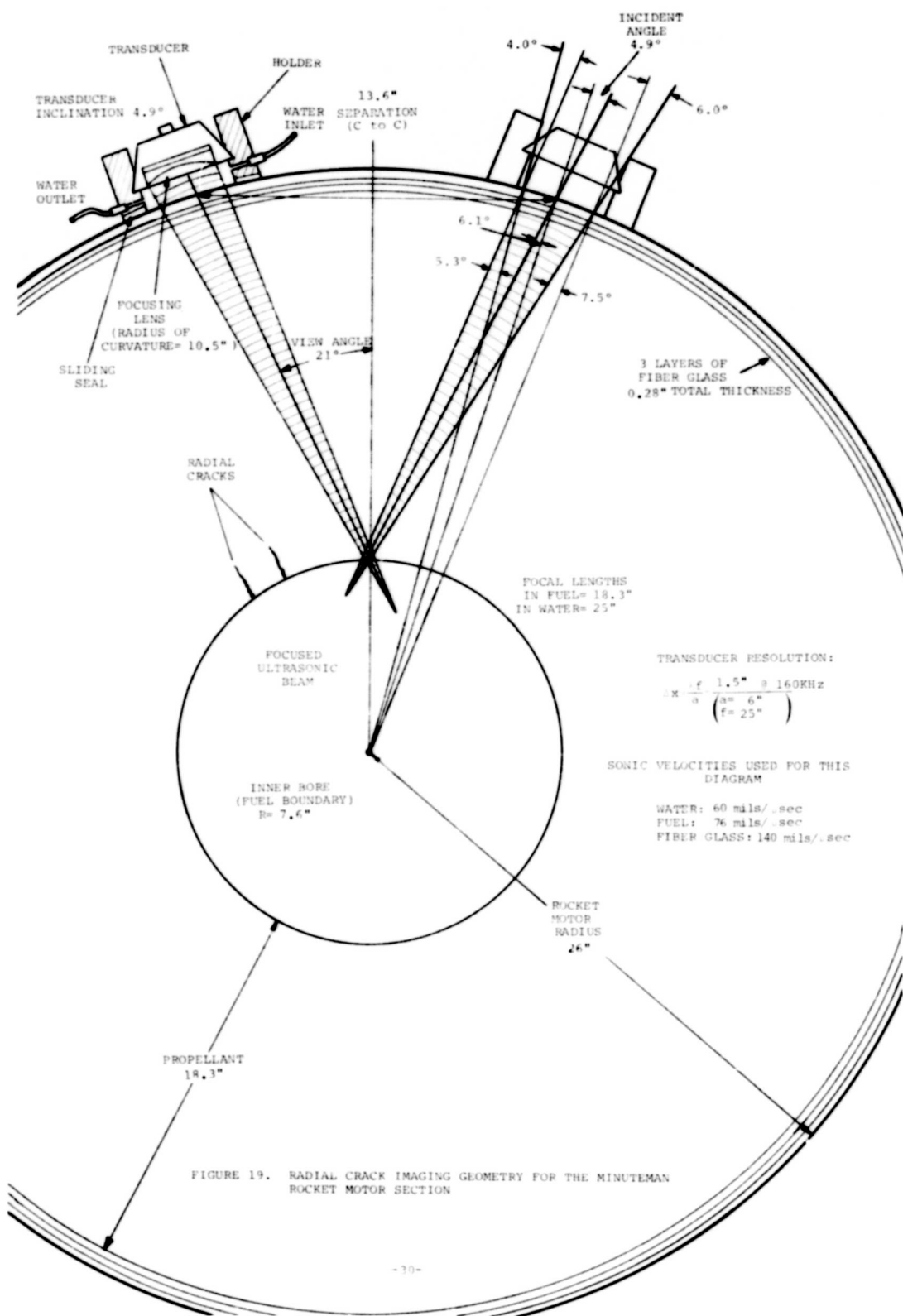


FIGURE 19. RADIAL CRACK IMAGING GEOMETRY FOR THE MINUTEMAN ROCKET MOTOR SECTION

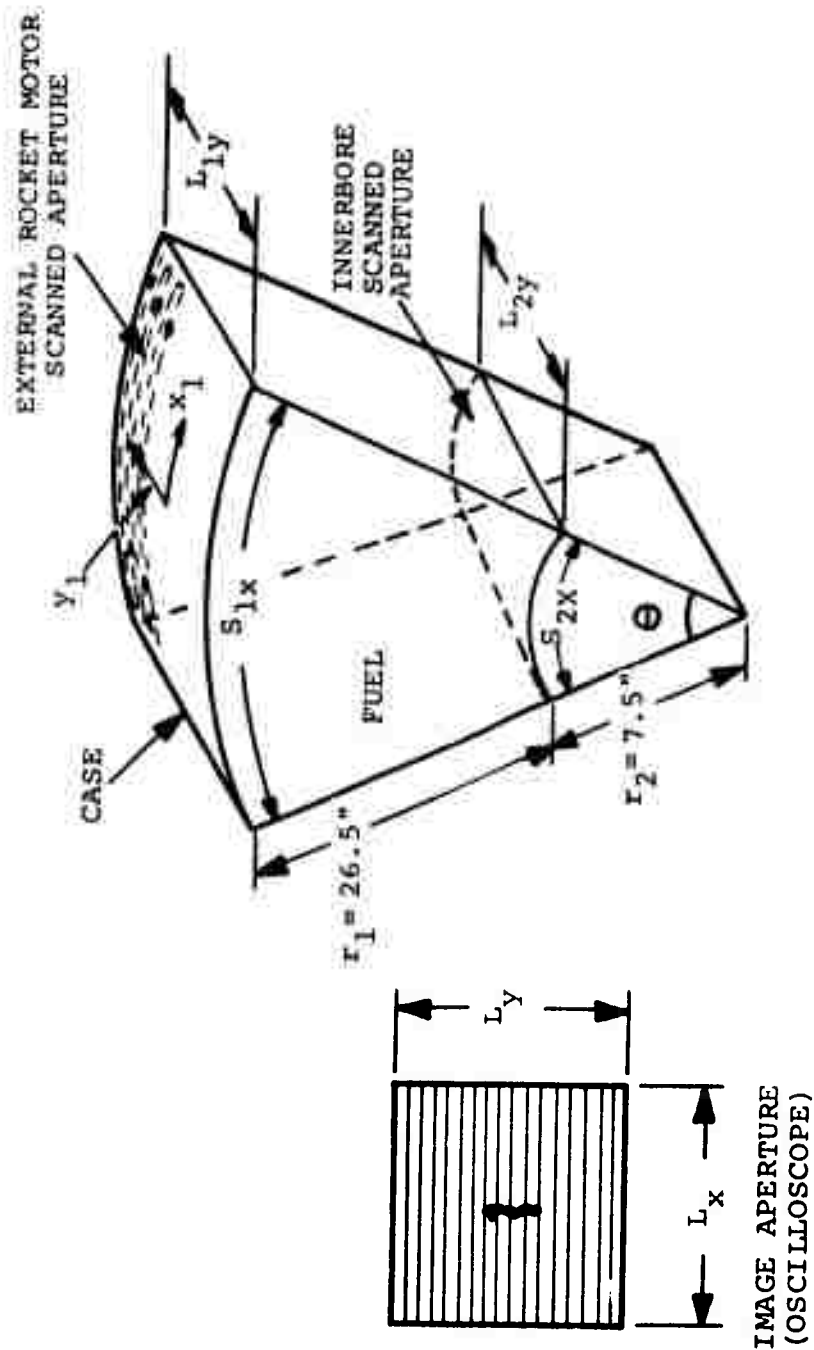


FIGURE 20. SCANNING APERTURE GEOMETRIES FOR THE MINUTEMAN  
ROCKET MOTOR SECTIONS

The aspect ratio of the display oscilloscope is determined by the following equation:

$$\frac{L_x}{L_y} = \left( \frac{r_2}{r_1} \right) \frac{S_{1x}}{L_{1y}} = \frac{S_{2x}}{L_{1y}} \quad (2)$$

where  $L_x$  = length of the image display aperture in the "x" direction,

$L_y$  = length of the image display aperture in the "y" direction

and  $L_{1y}$  = length of the scanned aperture in the "y" direction.

The aspect ratio ( $L_x/L_y$ ) was approximately 0.3 in the final imaging configuration. The image magnifications were 0.5 and 0.36 for the display scope and polaroid film, respectively.

### 5.5 *Image Resolution*

The concept and theory of image resolution has been the subject of many arguments and heated discussions. We hope to avoid all this by introducing and accepting the two point criterion of Lord Rayleigh from optics. Naturally, we will introduce some minor modification concerning coherent and incoherent illumination. In the final analysis, we hope the experimental data will verify the basic theory. The Rayleigh two-point resolution criterion has long been used as a quality factor for incoherent imaging systems. The theory will be restated in the following form.

### 5.6 *Rayleigh Resolution*

Two points are said to be resolved when the center of the Airy disk, produced by one object, falls on the first null ( $\alpha$ ) of the Airy disk generated by the second point. Figure 21 shows the two Airy patterns satisfying the Rayleigh criterion for incoherent illumination.

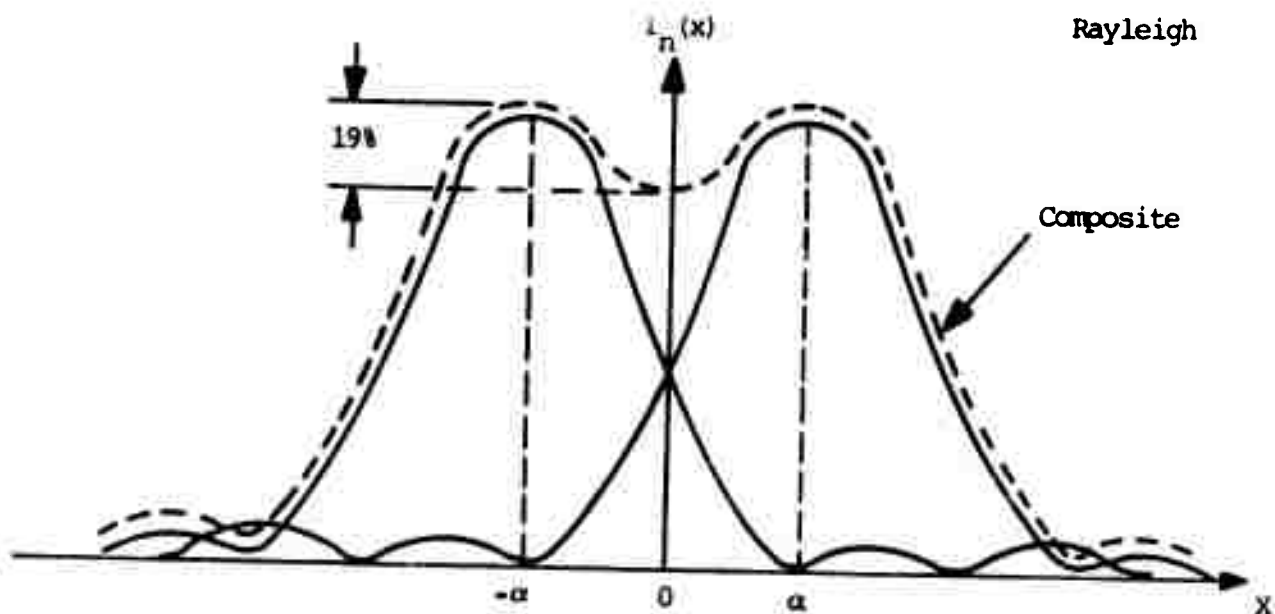


FIGURE 21. CROSS-SECTION OF TWO AIRY PATTERNS  
AT THE RAYLEIGH DISTANCE

The resolving power of an acoustical imaging system is, by our definition, the smallest lateral separation  $\Delta x$  below which two object points cannot be distinguished in the image. The composite pattern (Figure 21) shows a 19% dip that differentiates or resolves the two objects. If the points were closer together than  $\Delta x$ , the composite pattern would merge into one continuous peak and the objects would be unresolved. The lateral resolution  $\Delta x$  can then be defined by the following equation for a circular focused transducer:

$$\Delta x = 1.22 \frac{\lambda f}{a} \quad (3)$$

where  $\lambda$  = acoustic wavelength

$f$  = focal length

and  $a$  = lens diameter.

Now we must consider the effects of coherent insonification with respect to the Rayleigh criterion. Figure 22 is the composite pattern for two mutually coherent point sources separated at the Rayleigh distance.

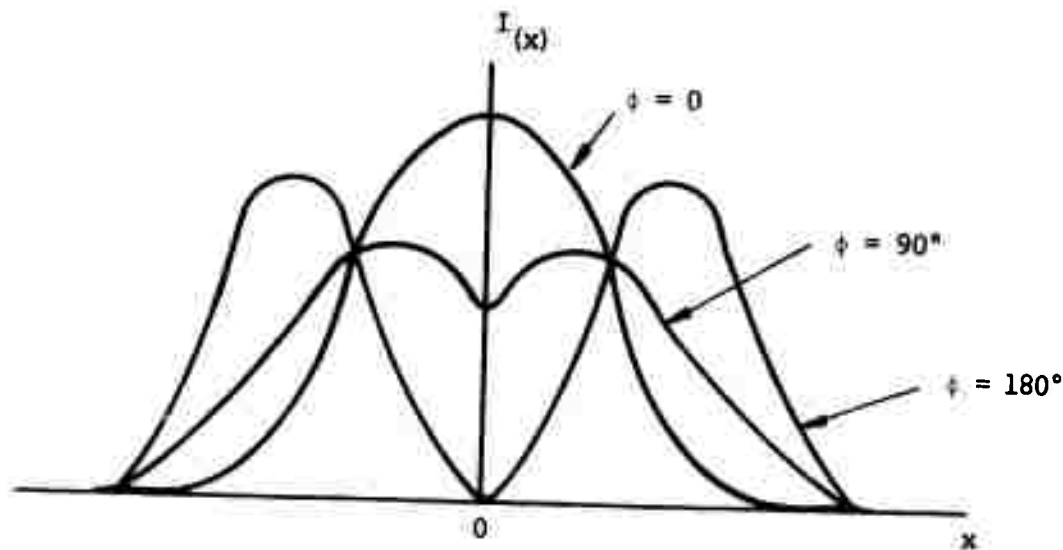


FIGURE 22. COMPOSITE INTENSITY PATTERNS OF TWO MUTUALLY COHERENT POINT SOURCES SEPARATED AT THE RAYLEIGH DISTANCE

The relative phase ( $\phi$ ) between the two sources dominates the resultant shape of the composite pattern. If both points have the same phase, they are no longer resolvable at the Rayleigh distance; but if in phase quadrature the pattern coincides identically with the incoherent pattern, the above results tend to negate the resolution theory for holography or coherent imaging. This last statement requires the modification we previously mentioned. In most practical applications, the source and receive transducers are not perfect points, but disks in the order of five to ten wavelengths. The rather crude points introduce many different ray paths to each point on the object. The resultant phase at the point is determined by the summation of all the phases as a result of the different path lengths. The average phase can usually be considered zero under these conditions. Thus, if we assume these assumptions are correct, the Rayleigh criterion is valid.

### 5.7 Resolution - (Experimental Results)

Figure 23 shows the typical geometry used in verifying the transducer resolution experimentally. Two point objects were located at the focal plane of the transducer and separated initially at the Rayleigh distance. The objects were 1 inch diameter styrofoam disks separated edge-to-edge 1 inch. The transducer focal length was 16 inches and the lens diameter 6 inches. The operating frequency was 182KHz and the wavelength in water approximately 0.32 inches.

The image is shown in Figure 24 and the two points are resolved at the Rayleigh distance. The objects were then separated half the Rayleigh distance and two points merged in the image and were unresolvable. The results were in excellent correlation with the theory under the above laboratory conditions. All of the transducers used in radial crack imaging were subjected to this test. The sphericity of the beam was also verified using holography techniques (i.e., circular symmetry of the zone plate).

### 5.8 Radial Crack Focused Holography Resolution Imaging

The send-receive imaging geometry was simulated with two 9 inch focal length transducers separated 6.3 inches. The resolution targets were 8.3 inches from the center of the send-receive array.

Figure 25 shows the geometry used in constructing the resolution image of two targets with slant angle illumination separated at the Rayleigh distance.

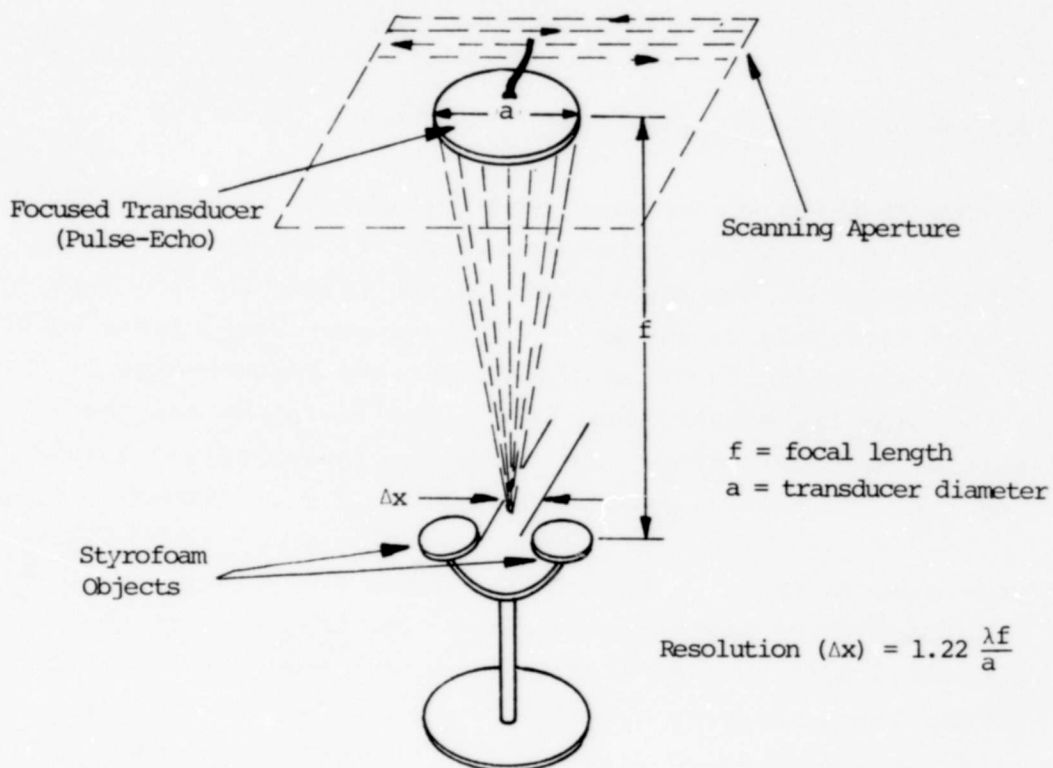


FIGURE 23. TWO POINT TRANSDUCER RESOLUTION GEOMETRY

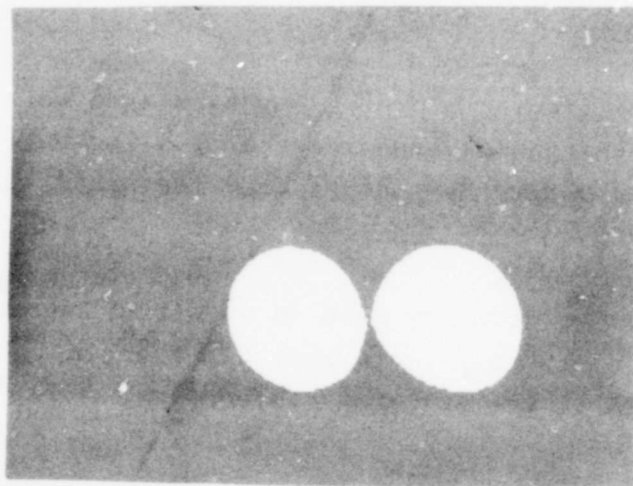


FIGURE 24. IMAGE OF TWO POINT OBJECTS SEPARATED AT THE RAYLEIGH DISTANCE



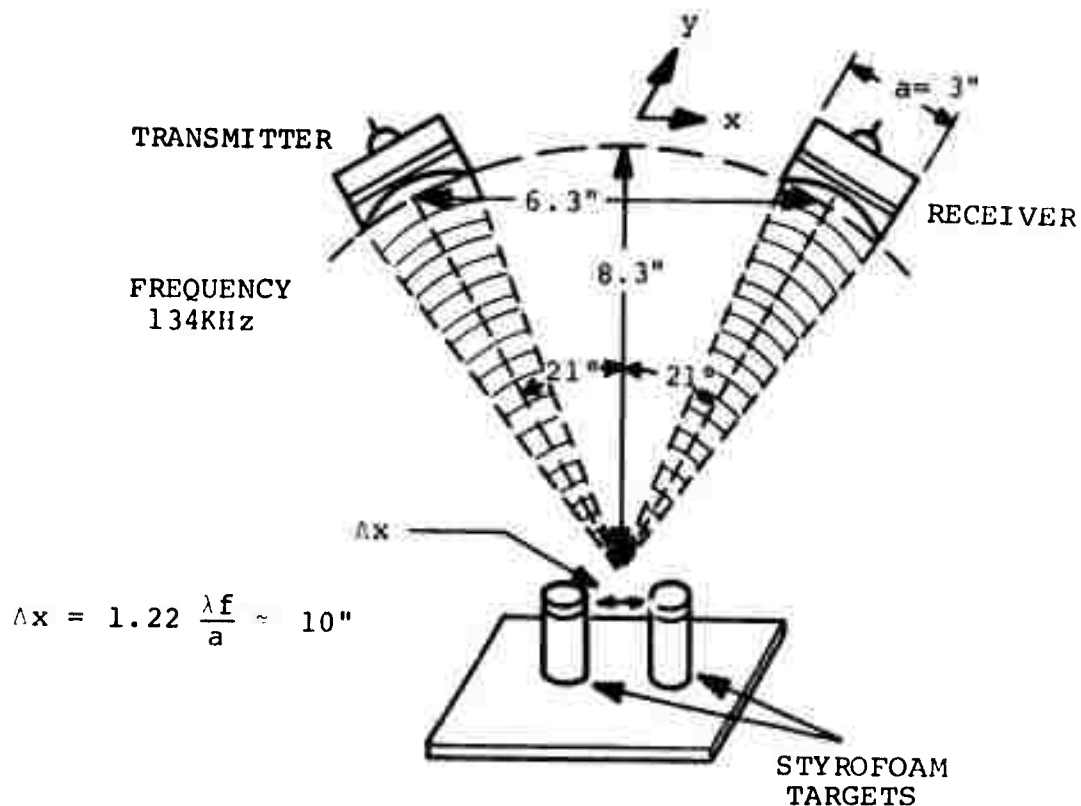


FIGURE 25. LABORATORY RESOLUTION GEOMETRY FOR  
SLANT ANGLE ILLUMINATION

The two transducers were scanned over a preselected aperture simulating the motor geometry. The image of the two point objects is shown in Figure 26. The image quality is excellent and the two objects are easily resolved at the Rayleigh separation.

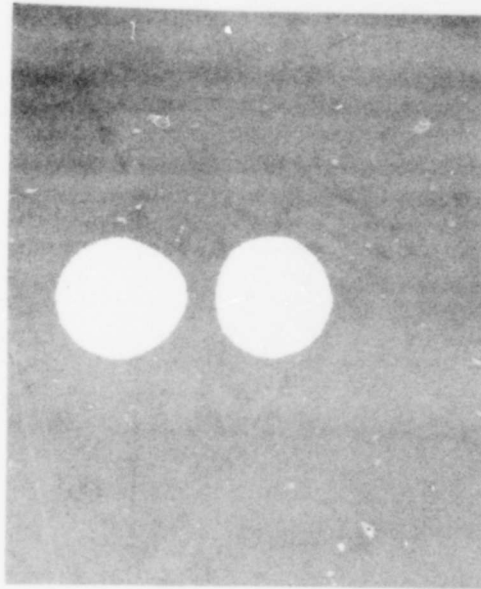


FIGURE 26. FOCUSED HOLOGRAM OF THE TWO 1 inch  
DIAMETER RESOLUTION OBJECTS  
Magnification: 0.46

The simulation was performed in water using a 0.44 inch wavelength. The theoretical resolution was approximately 1 inch with the above configuration.

#### 5.9 *Resolution Simulation Geometry for the Fiber Glass Case Sample*

Figure 27 shows the 48 inch diameter cylindrical tank with the plastic liner and the two resolution targets. The steel tank has a section removed for the scanned aperture. A fiber glass section has been inserted to simulate the external rocket motor case. The full scale mock up simulated the motor geometry with the exception of the propellant and various case material layers (i.e., rubber, etc.). The tank was filled with water to simulate the propellant.

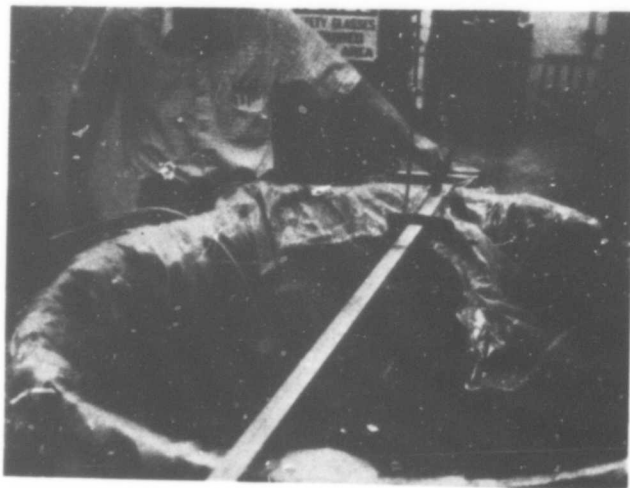


FIGURE 27. SIMULATION OF ROCKET MOTOR GEOMETRY  
WITH THE TWO RESOLUTION OBJECTS

The cylindrical scanner with the two plastic shoes, transducers, water coupling, etc. was mounted vertically against the external tank surface. The simulation was performed in preparation for the in situ imaging on the rocket motor sections in Yakima. The complete system was field tested using the water tank simulation.

Figure 28 is a schematic of the resolution geometry used in the simulation. Various views are depicted with the physical parameters to aid in the explanation and interpretation of the reconstructed images. The insonification frequency was 195KHz and the Rayleigh separation approximately 0.75 inch. The repetition or pulse frequency was 1.11KHz and the pulse length 150 $\mu$ s. These are typical values that were used in the in situ tests at Yakima. The acoustic energy was coupled through the fiber glass window into the interior of the tank as shown by the top view. The transducer array was scanned horizontally along the window and incremented vertically. The increment was  $0.67\lambda$  representing the sampling in the vertical direction and the horizontal sampling was well below the  $\lambda/2$  spacing.

# H<sub>2</sub>O SIMULATION EXPERIMENT

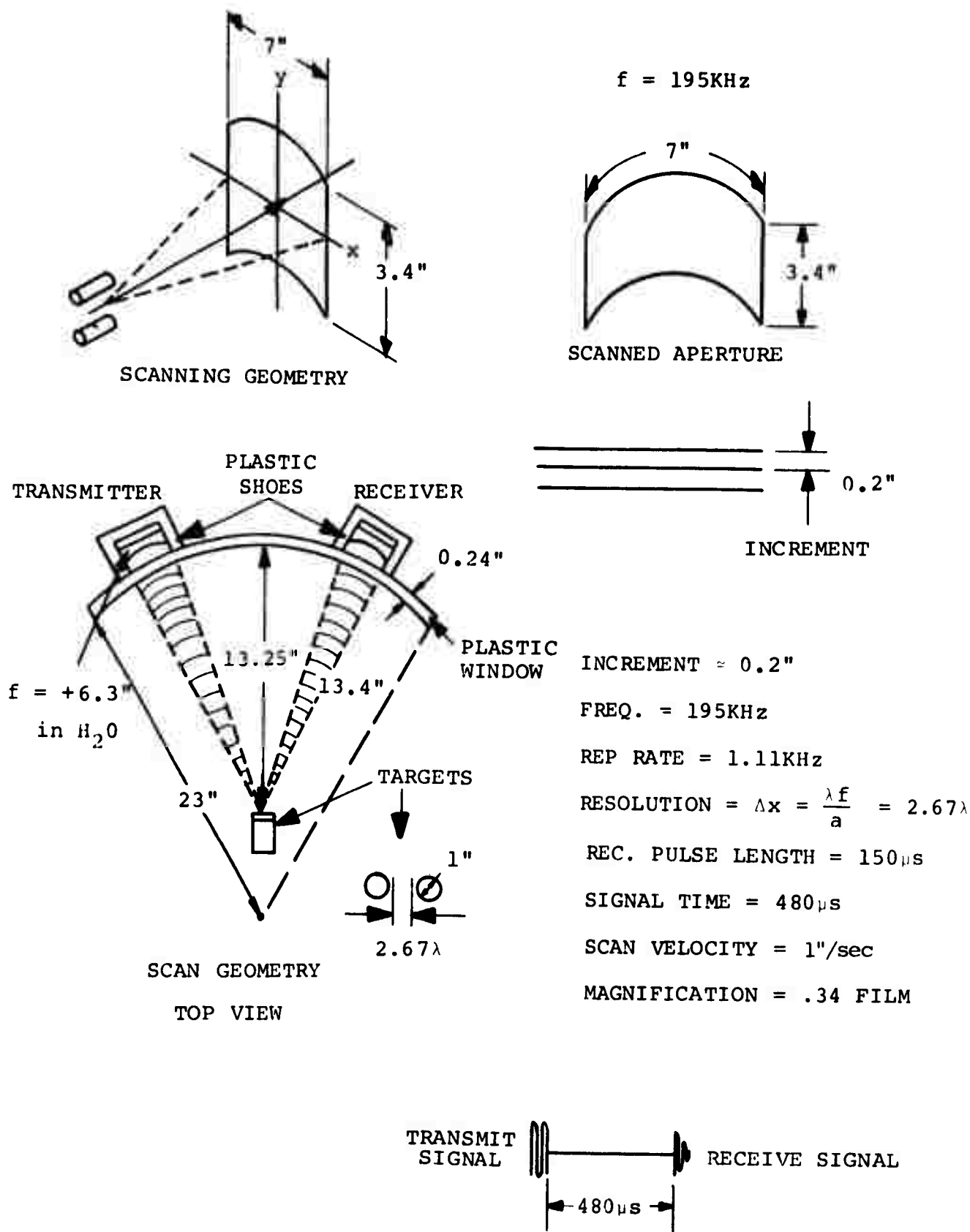
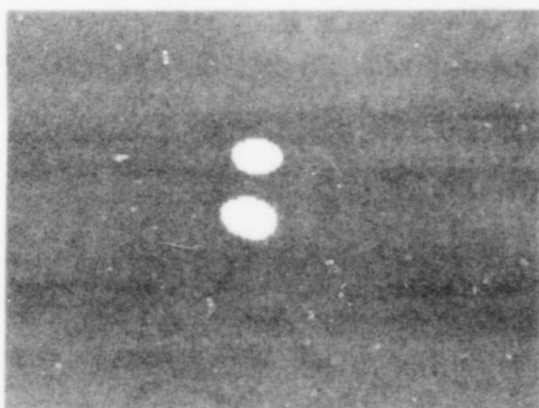
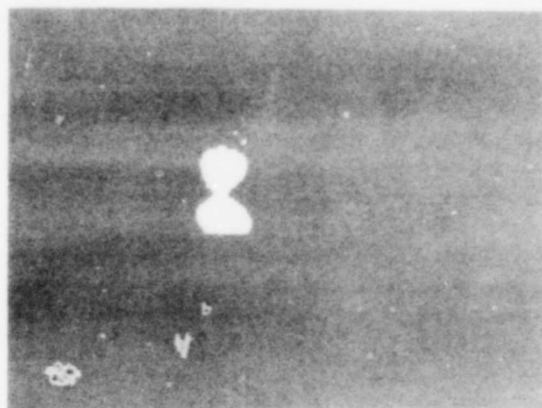


FIGURE 28. SCHEMATIC OF THE FOCUSED HOLOGRAPHY RESOLUTION GEOMETRY ON A SIMULATED MINUTEMAN ROCKET MOTOR

Figure 29a shows the focused hologram image of the two object points separated by the Rayleigh distance. The elliptical shapes indicate the presence of astigmatism in the image and this can be eliminated by aspect ratio adjustment. The two objects are again easily resolved in the



a



b

FIGURE 29. FOCUSED HOLOGRAMS OF THE TWO RESOLUTION OBJECTS IN THE ROCKET MOTOR SIMULATION TANK Magnification: 0.34

experimental mock-up. Figure 29b shows the image of two objects separated 0.75 of the Rayleigh distance. The image of the two objects have merged together indicating the two points are unresolvable. The two points could be considered resolvable in the image, but it is questionable, and thus we will stay with the Rayleigh criterion.

#### 5.10 *Simulated Radical Crack Imaging*

The image construction is shown in Figure 19 of the preceding section. The transducers were positioned to view the crack at approximately 21 degrees from the vertical. The two scanned overlapping directional focal patterns (transmit and receive) provide the viewing aperture. The

crack image resolution is essentially the Rayleigh criterion with modifications for the viewing angles.

Figure 30 shows the simulated crack defect emanating from the innerbore surface. The crack consisted of a metallic rectangle 0.5 inches in height and 2.75 inches in length. The innerbore surface is an aluminum sheet with the approximate innerbore missile radius of curvature. The simulated crack image was constructed in the tank with the fiber glass window.

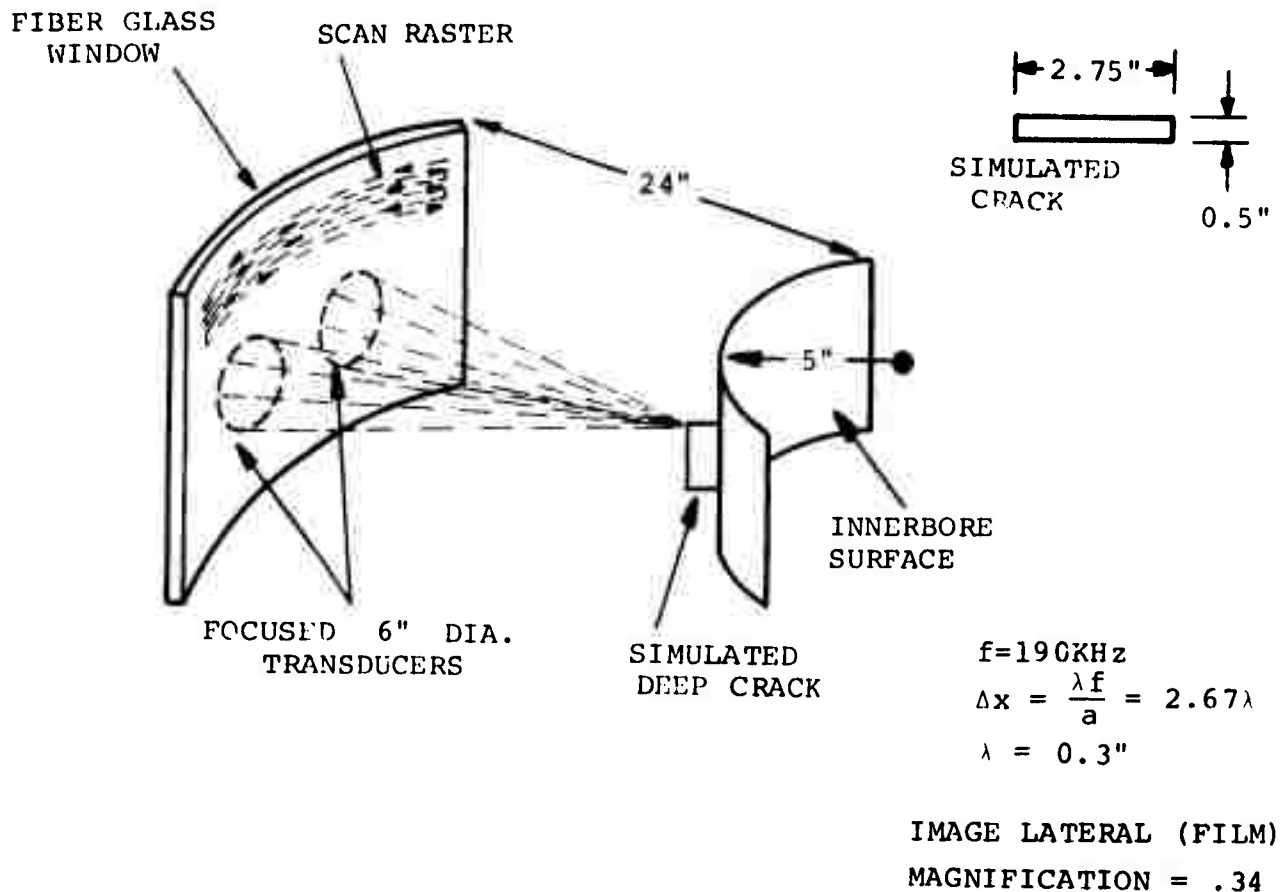
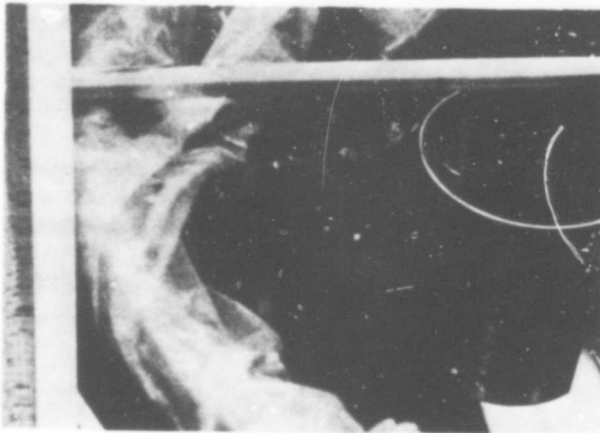
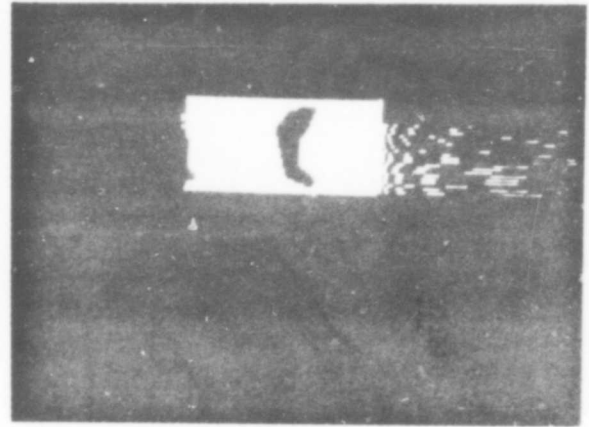


FIGURE 30. SIMULATED CRACK AND MOTOR SEGMENT GEOMETRY



a

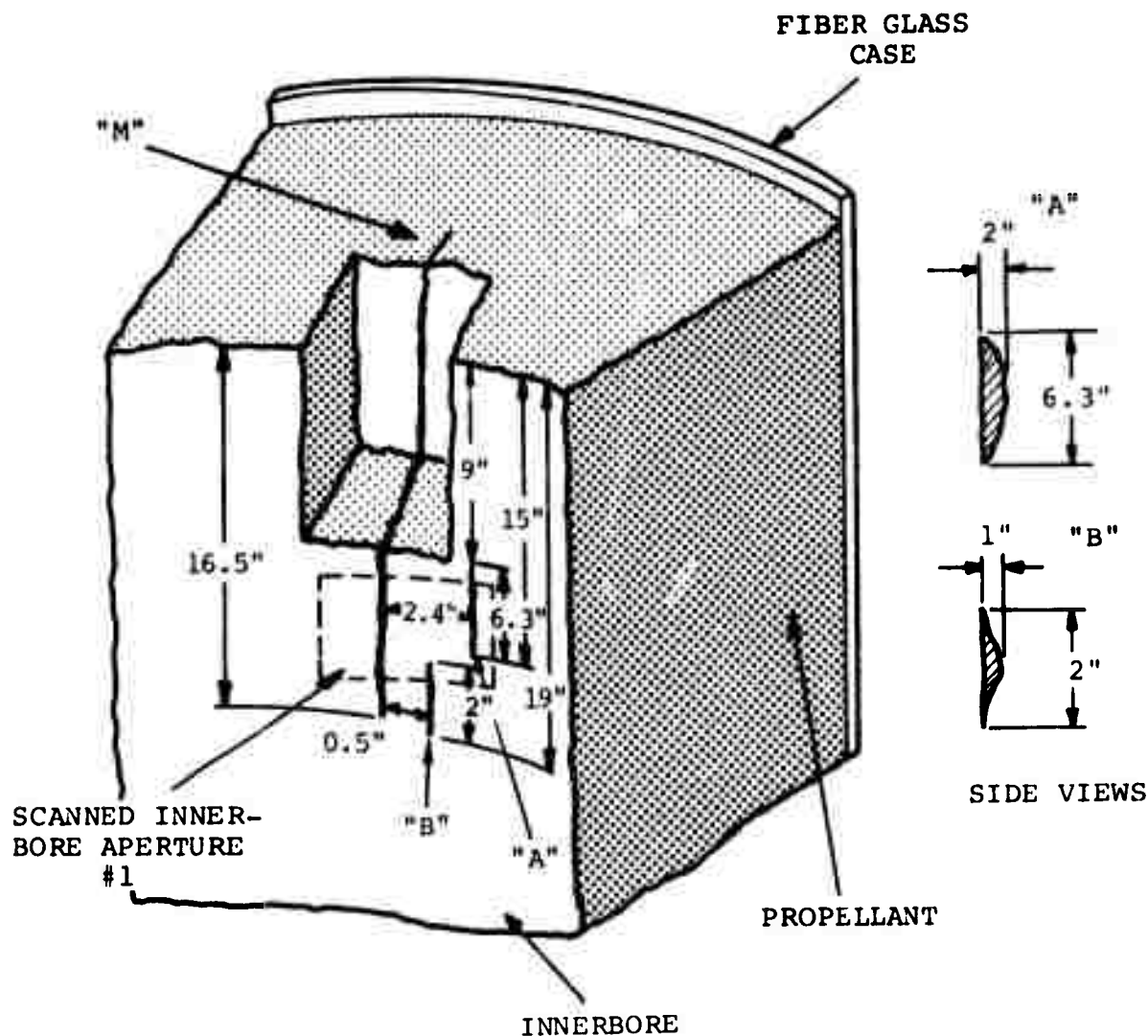


b

FIGURE 31. (a) SIMULATED CRACK ON MOTOR INNER-BORE AND (b) FOCUSED HOLOGRAM OF THE SIMULATED CRACK

Magnification: 0.34

Figure 31a shows the simulation mock-up of the innerbore crack in the tank. Figure 31a shows the focused hologram image of the simulated crack. The image magnification is 0.34 and the approximate resolution 0.75 inch. The apparent distortion is the result of the metal corners producing multiple reflections and mirror images. The two transducer geometry provides an excellent image of the radial crack with excellent resolution. Another simulated rectangular crack was constructed of styrofoam as shown in Figure 32a. The crack dimensions were reduced to 1 inch in length and 1.5 inches in width. The crack was suspended by two rods and placed at the focal plane of the two transducers. The focused hologram image was constructed through the fiber glass tank window. The innerbore surface was deleted and the crack image appears undistorted (see Figure 32a). The image is excellent indicating the interference was attributed to multiple reflections.



CRACK "M" PREVIOUSLY CONSTRUCTED

CRACKS "A" & "B" CONSTRUCTED BY HOLOSONICS

FIGURE 34.

INNERBORE CRACK GEOMETRY (MINUTEMAN ROCKET MOTOR SECTION)



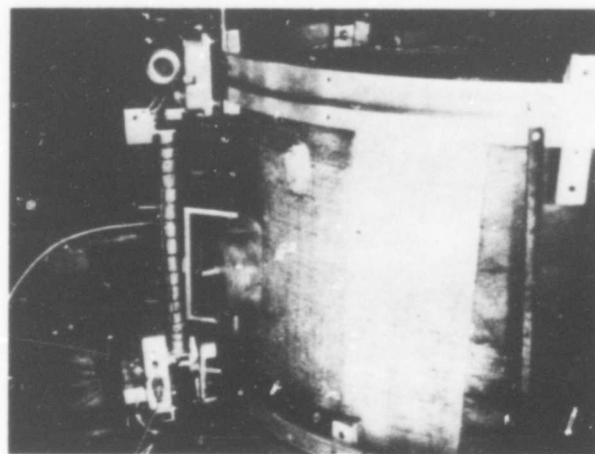
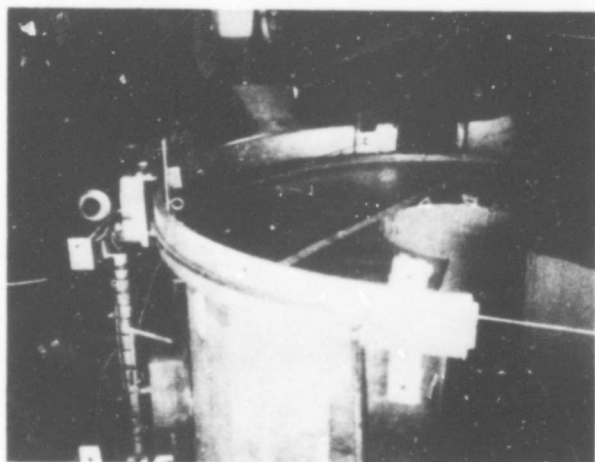
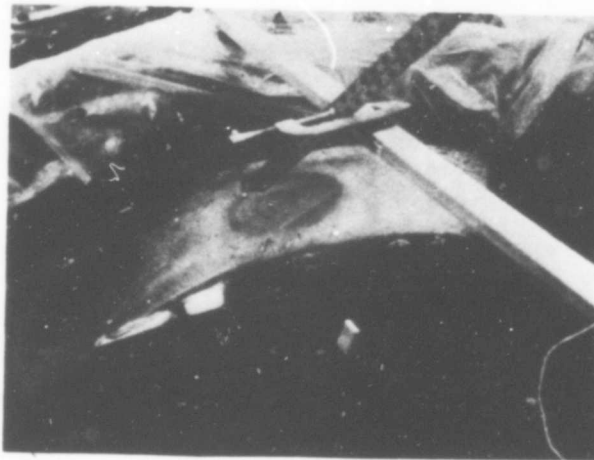
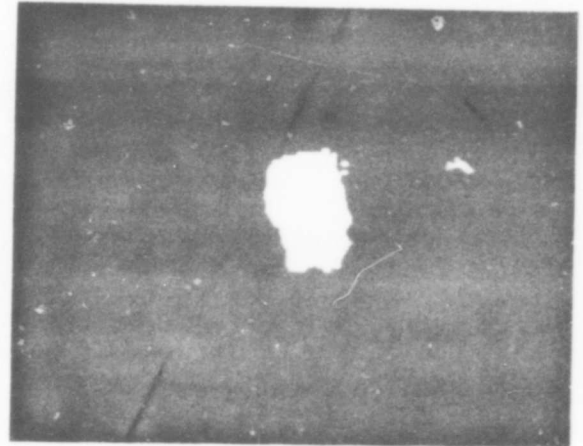


FIGURE 33. CYLINDRICAL SCANNER MOUNTED ON THE  
ROCKET MOTOR SECTION  
(Yakima, WA)

The holographic system and image geometry used in the construction of in situ radial cracks images have been described in the previous sections. Figure 34 illustrates the crack geometry as viewed from the innerbore. The crack designated "M" was already inserted prior to sample receipt. This crack was not discovered visually, but appeared when imaging crack "A" and "B". Cracks "A" and "B" were constructed by the insertion of a thin sharp knife. The crack surfaces merged together after removal of the blade and the actual thicknesses were less than 0.001 inches.



a



b

FIGURE 32. (a) SIMULATED STYROFOAM CRACK AND  
(b) FOCUSED HOLOGRAM OF THE SIMULATED  
CRACK

Magnification: 0.34

#### 5.11 *Radial Crack Imaging on Rocket Motor Sections at the Yakima Firing Center*

Figures 33(a,b) show two views of the cylindrical scanner mounted on the rocket motor section. One of the large 6 inch diameter transducers in the plastic housing is visible in the center of the aperture. The two drive motors (horizontal, vertical) are located on the upper track carriage. The upper and lower carriages are connected together by a central bar and threaded increment shaft. The complete unit scans a preselected cylindrical aperture on the external surface. The innerbore is visible in Figure 33a showing the small radius of curvature.

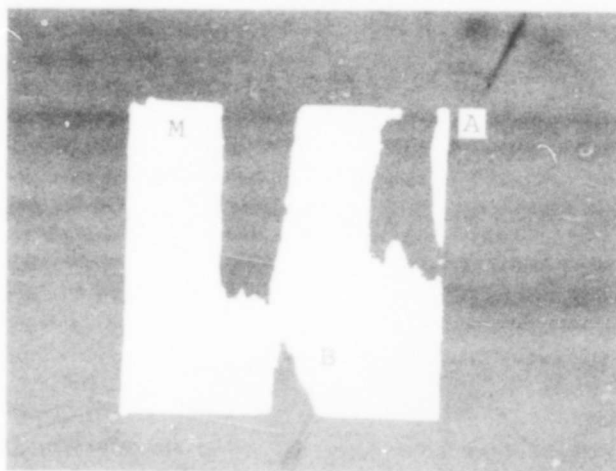
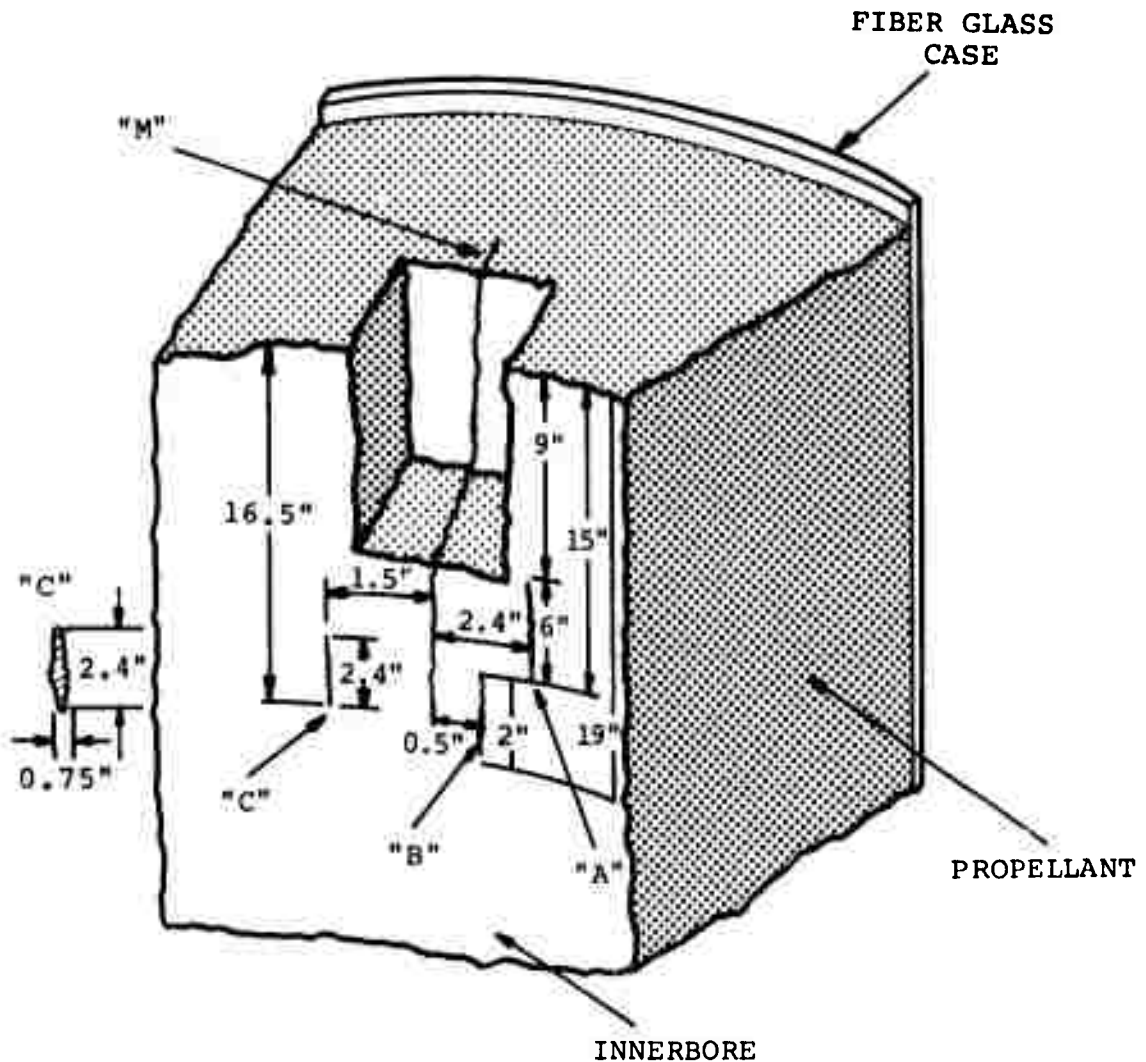


FIGURE 35. FOCUSED HOLOGRAM OF THE INNERBORE  
RADIAL CRACKS (APERTURE #1, FIGURE 34)  
Vertical Magnification: 0.34

Figure 35 shows the focused hologram of the crack "M" and the two smaller cracks ("A" and "B"). The hologram was constructed at 160KHz and the propellant wavelength was approximately 0.5 inches. The theoretical resolution was degraded to 1.8 inches as a result of transducer replacement. The 6 inch diameter transducers developed internal fatigue cracks between the lens-ceramic interface. The only available substitute was a smaller diameter ceramic (i.e., 4.75 inch diameter). The actual dimensions of "A" are 6.3 inches in length and approximately 2 inches in width. The only dimension available from the hologram for comparison with the actual dimensions is the width and it was 2 inches. The partial image of crack "B" is shown at the bottom of Figure 35. The complete length of "B" was missing because of aperture restrictions on the motor section. The prototype scanner was only capable of scanning within 8 inches of either surface (top or bottom). The approximate width of "B" varied from 0 to 1 inch. The maximum width dimension from the image was 1.3 inches. The actual dimensions of

crack "B" are 2 inches in length and variable in width (0 to 1 inch). The large crack "M" was not constructed by Holo-sonics and the actual dimensions are unknown. The width from the image dimension is approximately 2 inches.



CRACK "M" PREVIOUSLY CONSTRUCTED

CRACKS "A", "B" & "C" CONSTRUCTED BY HOLOSONICS

FIGURE 36. INNERBORE CRACK GEOMETRY (MINUTEMAN ROCKET MOTOR)

Figure 36 shows the identical innerbore surface as before with the exception of crack "C". The additional crack was constructed to evaluate shading. Figure 37 shows cracks "M", "A", "B" and "C". The partial image of "A" is shown on the extreme upper right of the aperture. The upper half of "B" is again shown at the bottom of the picture. "C", the new crack has its image merged with "M". The merging of two images is the result of shading (i.e., radial crack projection interference). The outline of "C" is easily identified by direct comparison with the previous image of "M" (see Figure 35). The effect of shading is the inability to differentiate individual cracks as shown in the two images.

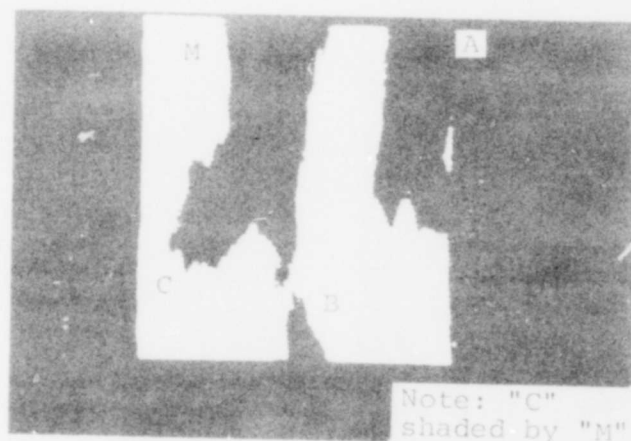


FIGURE 37. FOCUSED HOLOGRAM OF THE INNERBORE RADIAL CRACKS

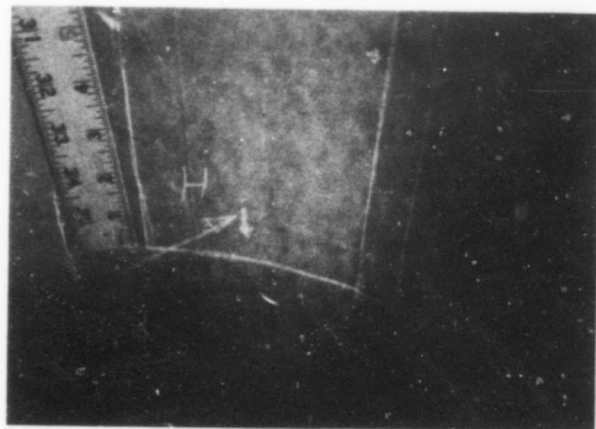
Vertical Magnification: 0.34

Horizontal Magnification: 0.20

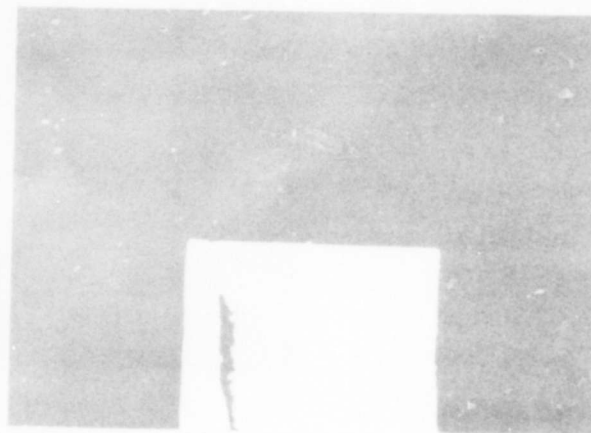
### 5.12 Radial Crack Imaging Sensitivity

The previous imaging results included cracks of various lengths and widths without defining any minimum detectable size. The initial efforts were to prove feasibility and minimum crack size was of secondary concern. Figure 38a shows the small innerbore crack as viewed from the inner-bore. The crack was constructed in a section of the missile that was relatively free of other defects. The crack dimensions were approximately 1 inch for the length and 0.5 inches in width.

The extremely small crack was below the system resolution, but hopefully we could detect it. The results are shown in Figure 38b and the sensitivity of the imaging system is sufficient to detect cracks in the order of one wavelength (i.e., 0.5 inches @160KHz).



a



b

FIGURE 38. (a) INNERBORE CRACK "H" AND  
(b) CRACK IMAGE

### 5.13 Simplified Radial Crack Image Analysis

Figure 39 shows the schematic of the innerbore crack geometry. If we use parallel geometrical optics and assume the acoustic ray theory is valid, the analysis will provide information on the crack's effective acoustic cross-section. The effect of curvature will be deleted from the analysis on the assumption the cracks are small in height (i.e., vertical dimension).

$h$  = (True Crack Height)

$h_a$  (Apparent Crack Height)

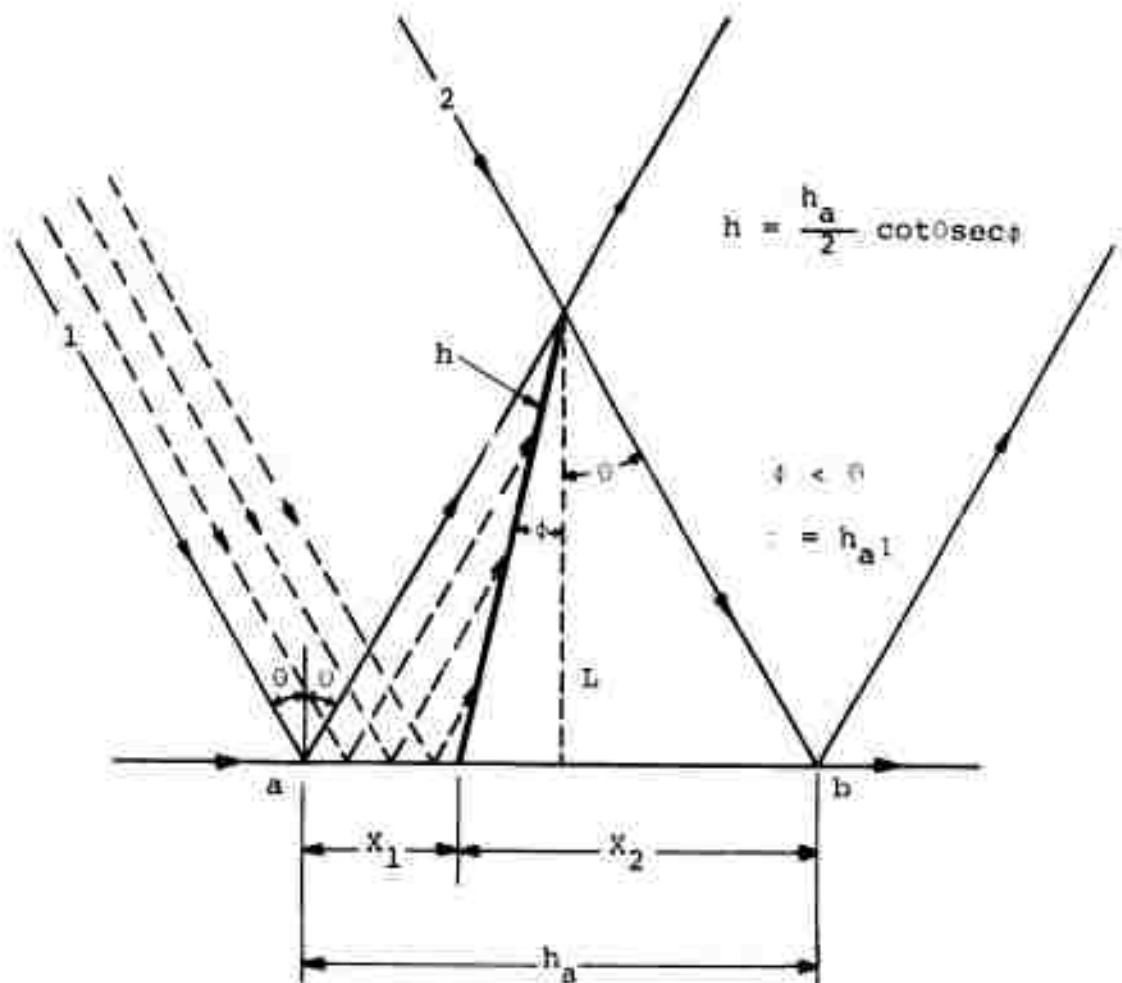


FIGURE 39. TRANSDUCER PATTERN CRACK GEOMETRY

The effective cross-section is defined as  $\sigma$  for the angles less than or equal to  $\theta$ . The focused transmitter rays between 1,2 are effectively blocked from the receiver. The other rays emerge unobscured and received by the receive transducer.

The sequence starts at "a" and terminates at "b" in Figure 39. The distance  $h_a$  is the effective line shadow of the crack. The cross-section  $\sigma$  is the product of  $h_a$  and the crack length.

The true crack height is given by the following equation:

$$h \approx 0.5 h_a \cot \theta \sec \phi$$

when  $\theta \approx 21^\circ$ .

This simple analysis neglects the conical shape of the transducer beams, diffraction effects, etc. It was included to aid in visualizing the interaction of the two beam patterns with the radial crack.



## SECTION 6

### CONCLUSIONS

The results of the program are very encouraging in that the experimental data indicates that acoustical holography techniques can be applied to nondestructive inspection of large solid rocket motors in situ.

Several areas require further study prior to development of the technique for application. They are:

6.1 *The imaging of bore cracks through titanium and steel case material.*

6.2 *The imaging of bore cracks through external insulations (e.g., cork, AVCOAT).*

6.3 *The imaging of debonds between fiber glass case material and propellant, and between steel and propellant.*

6.4 *The development of improved imaging transducers (axicons, etc.) with low f-numbers (i.e., large depth-of-field) for deep penetration imaging of cracks in propellant.*

6.5 *The development of a viable mechanical scanner for missile inspection.*

## REFERENCES

- 1) Heuter, T. F. and Bolt, R. H., Sonics, John Wiley & Sons, 1955.
- 2) Mcleod, J. H., "The Axicon: A New Type of Optical Element", J. Opt. Soc. Am. 44, 592-597 (1954).
- 3) Burckhart, C. B., Grandchamp, P. A. and Hoffman, H., Methods for Increasing the Lateral Resolution of B-Scan, Acoustical Holography Vol. 5, Editor Green, P. S. Plenum Press, 1973.
- 4) Burckhart, C. B., Ultrasound Axicon, J. Acoust. Soc Am 54, 1628, (1973).
- 5) Hildebrand, B. P. and Brenden, B. B., Introduction to Acoustical Holography, Plenum Press, New York, 1972.